공학박사학위논문

난류 채널 유동 내 벽면에 부착된 에디: 압력 섭동과 스케일 상호 작용

Attached eddies in turbulent channel flow: pressure fluctuations and scale interactions

2017 년 8 월

서울대학교 대학원

기계항공공학부

조 민 정

Attached eddies in turbulent channel flow: pressure fluctuations and scale interactions

Minjeong Cho
Department of Mechanical & Aerospace Engineering
Seoul National University

Abstract

The multi-scale behavior of eddies in wall-bounded turbulent flows has hindered understanding of their nature. However, in the present study, statistical and dynamical features of wall-bounded turbulent flows are explored with a modern view of coherent structures in wall turbulence, incorporating Townsend's attached eddy hypothesis. Through this analysis, the ultimate goal is to elucidate the mechanism for the maintenance of wall turbulence.

In Part I, numerical experiments isolating an attached eddy only at a prescribed spanwise length scale are performed to examine characteristics of pressure fluctuations of self-sustaining attached eddies. The pressure field of each attached eddy is statistically and dynamically self-similar with respect to the corresponding spanwise size, implying that structures of pressure fluctuations indeed emerge in the form of Townsend's attached eddies. Also, time sequences obtained from minimal unit simulations show that both rapid (linear) and slow (nonlinear) pressure fluctuations are amplified together with the streamwise meandering streaks in the self-sustaining cycle.

In Part II, large eddy simulation of turbulent channel flow is conducted to clarify the scale-by-scale interactions. From energy spectra of each constituent

of the turbulent kinetic energy equation in wavenumber space along with analyses of scale interactions, a comprehensive view of the energy transfer mechanism is described. Turbulent kinetic energy produced by the lift-up effect in the self-sustaining process of attached eddies is absorbed by the negative turbulent transport energy originating from nonlinear interactions between larger attached eddies. Then, the absorbed energy is transported to the region where the turbulent transport spectra have a positive value via the energy cascade and dissipated there. The energy redistribution mechanism through the pressure-strain term has also been shown to the self-sustaining process of attached eddies. Therefore, the dominant mechanism for the maintenance of wall turbulence is revealed as the self-sustaining process of attached eddies at each length scale.

Keywords: attached eddy, pressure fluctuations, scale interactions, turbulent kinetic energy, self-sustaining process, turbulent channel flow

Student number: 2011-22897

Contents

List of Figures

Part I. Pressure fluctuations of attached eddies

Figure

Part II. Scale interactions in turbulent channel flow

List of Tables

Part I. Pressure fluctuations of attached eddies

Table

Nomenclature

Roman Symbols

a, b, c	Various sizes of attached eddies, see table 2.1
C_{ij}	Time correlation function
C_s	Smagorinsky constant
D/Dt	Material time derivative
E_{p_r}	Energy of rapid pressure fluctuations
E_{p_s}	Energy of slow pressure fluctuations
E_u	Energy of streamwise velocity fluctuations
E_v	Energy of wall-normal velocity fluctuations
E_w	Energy of spanwise velocity fluctuations
E_0	Energy of streamwise uniform component of motions at the smallest spanwise wavenumber ($k_x = 0$ and $k_z = 2\pi/L_z$)
E_1	Energy of the smallest wavenumber components ($k_x = 2\pi/L_x$ and $k_z = 2\pi/L_z$)
e	Turbulent kinetic energy
F	Full simulation, see table 2.1
h	Channel half-height
k_x	Streamwise wavenumber
k_z	Spanwise wavenumber
$k_{z,0}$	Spanwise wavenumber at a given point in $y - \lambda_z$ plane
L	Simulation of self-sustaining attached eddy in the log layer, see table 2.1
L_x	Streamwise domain size

L_y	Wall-normal domain size
L_z	Spanwise domain size
l	Spanwise wavenumber ($l + m = k_z$), see equation (3.2) in Part II
ML	Simulation of self-sustaining minimal attached eddy in the log layer, see table 3.1
m	Spanwise wavenumber ($l + m = k_z$), see equation (3.2) in Part II
N_x	Number of grid points in x direction
N_y	Number of grid points in y direction
N_z	Number of grid points in z direction
P	Production of turbulent kinetic energy
p	Pressure
$p_f = p$	Full pressure
p_r	Rapid pressure
p_s	Slow pressure
p_{st}	Stokes pressure
Q	Second invariant of the velocity gradient tensor
Re	Reynolds number
Re_m	Reynolds number based on the bulk mean velocity
Re_τ	Reynolds number based on the wall-shear velocity
T	Averaging time
T_p	Pressure transport of turbulent kinetic energy
T_{turb}	Turbulent transport of turbulent kinetic energy
$T_{turb,x}$	Turbulent transport of turbulent kinetic energy in x direction
$T_{turb,y}$	Turbulent transport of turbulent kinetic energy in y direction
$T_{turb,z}$	Turbulent transport of turbulent kinetic energy in z direction

T_ν	Viscous transport of turbulent kinetic energy
$T_{\nu,x}$	Viscous transport of turbulent kinetic energy in x direction
$T_{\nu,y}$	Viscous transport of turbulent kinetic energy in y direction
$T_{\nu,z}$	Viscous transport of turbulent kinetic energy in z direction
t	Time
U	Mean streamwise velocity
$u'(= u'_1)$	Streamwise velocity fluctuations
$u(= u_1)$	Streamwise velocity
u_τ	Wall-shear velocity
$\overline{u'v'}$	Reynolds stress
V_h	Volume of Ω_h
$v'(= u'_2)$	Wall-normal velocity fluctuations
$v(= u_2)$	Wall-normal velocity
$w'(= u'_3)$	Spanwise velocity fluctuations
$w(= u_3)$	Spanwise velocity
$x(= x_1)$	Streamwise coordinate
$y(= x_2)$	Wall-normal coordinate
y_0	Wall-normal location at a given point in $y - \lambda_z$ plane
$z(= x_3)$	Spanwise coordinate

Greek Symbols

Δx	Grid spacing in x direction
Δy	Grid spacing in y direction
Δz	Grid spacing in z direction
$\Delta\tau$	Phase difference
δ	Outer length scale, boundary layer thickness

δ_ν	Inner length scale, ν/u_τ
ε	Viscous dissipation of turbulent kinetic energy
ε_x	Viscous dissipation of turbulent kinetic energy in x direction
ε_y	Viscous dissipation of turbulent kinetic energy in y direction
ε_z	Viscous dissipation of turbulent kinetic energy in z direction
ε_{SGS}	Subgrid-scale dissipation of turbulent kinetic energy
$\varepsilon_{SGS,x}$	Subgrid-scale dissipation of turbulent kinetic energy in x direction
$\varepsilon_{SGS,y}$	Subgrid-scale dissipation of turbulent kinetic energy in y direction
$\varepsilon_{SGS,z}$	Subgrid-scale dissipation of turbulent kinetic energy in z direction
η	Kolmogorov length scale
λ_x	Streamwise wavelength
λ_z	Spanwise wavelength
$\lambda_{z,0}$	Prescribed spanwise length scale of attached eddies
ν	Kinematic viscosity
Π_x	Pressure strain of turbulent kinetic energy in x direction
Π_y	Pressure strain of turbulent kinetic energy in y direction
Π_z	Pressure strain of turbulent kinetic energy in z direction
τ_{ij}	Subgrid-scale stress
Ω_h	Lower (or upper) half of the computational domain of integration
$\Omega_{y,h}$	Lower (or upper) half of the wall-normal computational domain of integration
ω_x	Streamwise vorticity
ω_y	Wall-normal vorticity

Other symbols

$\hat{(\,)}$	Fourier coefficient
$\bar{(\,)}$	Average over x, z and t
	also average over t for chapters 3 and 4 in Part II
$\tilde{(\,)}$	Filtered quantity, see equation (2.5) in Part I
$(\,)'$	Fluctuations
$(\,)^+$	Quantity normalized by the wall variables
$(\,)^*$	Complex conjugate
$< >$	Average over t, see equation (3.2) in Part I
$< >_x$	Average over x
$(\,)_{max}$	Maximum value
$(\,)_{rms}$	Root-mean-square value
$(\,)_{wall}$	Value at the wall

Abbreviations

DNS	Direct numerical simulation
DSM	Dynamic Smagorinsky model
LES	Large eddy simulation
LSM	Large-scale motion
SGS	Subgrid-scale
TKE	Turbulent kinetic energy
VLSM	Very-large-scale motion
rms	Root-mean-square

Part I

Pressure fluctuations of attached eddies

Chapter 1

Introduction

Understanding pressure fluctuations in turbulent flows is an important issue in engineering applications as they induce noise generations and structural vibrations. Also, as the pressure at a given location is determined by corresponding velocity field of the entire computational domain through Poisson equation, it may also be important to develop effective flow control method (Kim, 1989; Luhar *et al.*, 2014). Pressure strain terms are also important, due to their role of redistributing turbulent kinetic energy to different flow directions and their applicability to the turbulence modeling. Despite this importance, because of the difficulty of measuring fluctuating pressure especially inside the boundary layer (Tsuji *et al.*, 2007), the understanding of the nature of pressure fluctuations is much lower than that of velocity fluctuations. Starting from the pioneering work of Kim (1989), which performed a direct numerical simulation (DNS) of turbulent channel flow at $Re_\tau = u_\tau h/\nu \simeq 180$, where u_τ is wall-shear velocity, h is channel half-height and ν is kinematic viscosity, Jiménez & Hoyas (2008) reported statistical behavior of pressure fluctuations up to $Re_\tau \simeq 2000$. Recent development of experimental techniques leads Tsuji *et al.* (2007) and Klewicki *et al.* (2008) to investigate the pressure fluctuations in turbulent boundary layer up to $Re_\tau \simeq 4000$ and 10^6, respectively. While the above studies focused on statistical features of pressure fluctuations, a recent study of Luhar *et al.* (2014) explored the structural nature and origin of pressure

fluctuations in the framework of resolvent analysis. However, even though they provided informative results such as a possibility of an amplitude modulation in the pressure field, the resolvent analysis essentially yields the rapid (linear) pressure fluctuations, which indicates the linear interaction of the velocity fluctuation with mean shear. It is well known that the slow (nonlinear) pressure fluctuations originating from nonlinear interactions between the velocity fluctuations are dominant throughout the flow field (Kim, 1989; Jiménez & Hoyas, 2008) and in this respect, Jiménez (2013) pointed out the incompleteness of the linearized Navier-Stokes equations based approach.

With the viewpoint of the attached eddy hypothesis (Townsend, 1961, 1976; Perry & Chong, 1982), it may be possible to elucidate the dynamical features of the pressure fluctuations in wall turbulence. The concept of attached eddy was first proposed by Townsend (1961, 1976), who inferred that the size of energy-containing motions in the logarithmic layer would be proportional to the distance of their centers from the wall. In this way, these attached eddies connect the inner length scale $\delta_\nu = \nu/u_\tau$ in the viscous wall layer and the outer length scale δ in the outer layer (Hwang, 2015). In other words, the coherent structures are attached to the wall, forming a hierarchy as illustrated by Perry & Chong (1982) (see figure 1.1). Based on this hypothesis, Townsend (1976) suggested theoretical predictions for turbulent fluctuations in the logarithmic layer derived from the random superposition of various sizes of self-similar attached eddies with a probability distribution function which allows constant Reynolds stress in the logarithmic layer. That is, streamwise and spanwise components of velocity fluctuations and pressure fluctuations would have a logarithmic distribution with respect to the wall-normal direction, while the wall-normal velocity fluctuations do not exhibit a log dependence as it is derived under the assumption of the impermeability condition. Various stud-

ies have reported the logarithmic behavior of streamwise and spanwise velocity fluctuations either experimentally (Kunkel & Marusic, 2006; Marusic *et al.*, 2013) or numerically (Jiménez & Hoyas, 2008; Lee & Moser, 2015). Especially, Jiménez & Hoyas (2008) clearly showed the logarithmic regions of pressure fluctuations. Also, the presence of attached eddies, which is a fundamental concept of the hypothesis, has been recently revealed. Hellström *et al.* (2016) experimentally showed the self-similarity of the energy-containing eddies in turbulent pipe flow with proper orthogonal decomposition analysis. Furthermore, recent numerical experiments which simulate the attached eddies only at a prescribed spanwise length scale showed that the computed statistics are self-similar with respect to their spanwise length scale (Hwang, 2015). It was also revealed that a single attached eddy was composed of long streaky motions and streamwise vortical structures, where the smallest one is the near-wall streaks and quasi-streamwise vortices (Kline *et al.*, 1967; Kim *et al.*, 1987; Hamilton *et al.*, 1995), while the largest one corresponds to very-large-scale motions and large-scale motions (Kim & Adrian, 1999; Hutchins & Marusic, 2007; Monty *et al.*, 2009).

Recently, a self-sustaining nature of attached eddies was further investigated by Hwang & Bengana (2016). It was reported that attached eddies in the form of long streaky structures and streamwise vortical structures in the logarithmic or outer layer also undergo the well-known self-sustaining process originally suggested for the near-wall structures (Hamilton *et al.*, 1995; Schoppa & Hussain, 2002). With these increased understanding of the general organization and sustaining mechanism of the coherent structures in wall-bounded turbulence, the objective of present study is to investigate the statistical and dynamical features of pressure fluctuations of the attached eddies by extending the scope of the previous studies by Hwang (2015) and Hwang & Bengana (2016). Firstly, the self-similarity of both rapid and slow pressure fluctuations

and their structures are explored. Then, the dynamics of each component of pressure fluctuations are examined in minimal unit simulations. In particular, to elucidate the pressure amplification process, their relation to the self-sustaining process is analyzed in detail.

This paper is organized as follows. Numerical methods for computing pressure fluctuations of self-sustaining attached eddies and results of the preliminary test are introduced in chapter 2. In chapter 3, statistical and dynamical features of computed pressure fluctuations of attached eddies are described and discussion is followed in chapter 4. This part concludes in chapter 5.

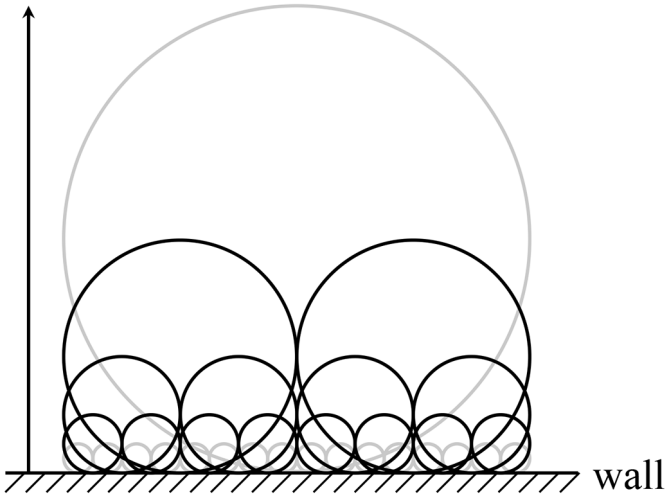

Figure 1.1. A conceptual sketch of the attached eddy hypothesis (Townsend, 1976; Perry & Chong, 1982). Black circles represent attached eddies in the logarithmic region, filling in the length scale separation between the smallest and the largest attached eddies (Hwang, 2015).

Chapter 2

Numerical methods

2.1 Large eddy simulation

Large eddy simulations (LES) of turbulent channel flows are conducted for the present numerical experiments (see figure 2.1 for flow configurations). The Navier-Stokes equations are in the form of evolution equations for the wall-normal vorticity and Laplacian of the wall-normal velocity (Kim *et al.*, 1987). Dealiased Fourier expansions are used in the streamwise ($x = x_1$) and spanwise ($z = x_3$) directions, and Chebychev polynomial expansions are used in the wall-normal ($y = x_2$) direction. The time advancement is carried out by a second-order semi-implicit scheme using a second-order Crank-Nicolson method for the diffusion terms and a third-order Runge-Kutta method for the convection terms. The streamwise, wall-normal and spanwise velocity components are indicated as $u\,(= u_1)$, $v\,(= u_2)$ and $w\,(= u_3)$, respectively. A constant mass flux is imposed by integrating zero wavenumber components of u and w separately. The constant Smagorinsky eddy viscosity model is used as a subgrid-scale (SGS) model, with the van Driest damping function (Härtel & Kleiser, 1998).

2.2 Computation of attached eddies at a given spanwise length scale

To isolate the attached eddies at a given spanwise length scale ($\lambda_{z,0}$), Hwang (2015) showed that the motions larger than the given one ($\lambda_z > \lambda_{z,0}$), where λ_z

is spanwise wavelength, can be removed by setting the spanwise domain size as $L_z = \lambda_{z,0}$ as shown in figure 2.1 and utilizing explicit filtering technique to filter out the motions which are uniform along the spanwise domain (i.e. $k_z = 0$): the right-hand side of x and y components of the momentum equations for $k_x \neq 0$ and $k_z = 0$ is set to zero, at each Runge-Kutta substep. Here, k_x and k_z denote the streamwise and spanwise wavenumbers, respectively (see Hwang (2013, 2015) for further details). Since the present solver is written in the form of the wall-normal vorticity (ω_y) and Laplacian of the wall-normal velocity ($\nabla^2 v$), the explicit filtering technique is applied as follows:

$$\hat{u}\,(y, k_x \neq 0, k_z = 0) = 0,\ \hat{v}\,(y, k_x \neq 0, k_z = 0) = 0, \tag{2.1}$$

where $\hat{u}$ and $\hat{v}$ indicate Fourier-transformed streamwise and wall-normal velocity components, respectively. Then, ω_y and $\nabla^2 v$ are updated at each Runge-Kutta substep. Additionally, the motions smaller than the given one ($\lambda_z < \lambda_{z,0}$) are damped out by conducting over-damped LES with increased Smagorinsky constant (C_s), as it is formulated in a purely dissipative form and does not transfer energy to the resolved quantities (Hwang & Cossu, 2010, 2011; Hwang, 2015). Note that increasing the C_s value has the same effect as increasing the filter width used for LES (Mason & Callen, 1986; Hwang, 2015).

Table 2.1 shows simulation parameters of present numerical experiments. Here, a case starting with F indicate full (reference) simulations using dynamic Smagorinsky model (DSM), which refers to conventional channel flow simulations without any artificially removed eddies. The remaining cases starting with L are simulations of attached eddies in the logarithmic layer: various spanwise length scales ($\lambda_{z,0} = L_z$) of self-sustaining attached eddies are computed at $Re_m = 38133, 73333$, where Re_m indicates Reynolds number based

Case	Re_m	Re_τ	L_x/h	L_z/h	$N_x \times N_y \times N_z$	C_s	Δx^+	Δz^+	Δy^+
$F1600$	73333	1668	8π	3	512×145×128	-	82	39	0.40 – 36
$L900a$	38133	878	12π	0.75	384×91×16	0.2	86	41	0.53 – 31
$L900b$	38133	912	12π	1	384×91×24	0.25	90	38	0.56 – 32
$L1600a$	73333	1439	8π	0.375	512×145×16	0.2	71	34	0.34 – 31
$L1600b$	73333	1602	8π	0.5	512×145×24	0.3	79	33	0.38 – 35
$L1600c$	73333	1800	8π	0.75	512×145×32	0.4	88	42	0.43 – 39

Table 2.1. Parameters for the reference simulations and simulations of self-sustaining attached eddies.

on the bulk mean velocity. Note that the filter (equation (2.1)) is applied to the cases starting with L. Re_m, computational domain sizes, grid spacings in wall-parallel directions (after dealiasing) and Smagorinsky constants are same as those of Hwang (2013, 2015), while slightly more grid points are used in the wall-normal direction due to different spatial discretization technique implemented in the present solver: Chebychev polynomial expansions in the present study and second-order central difference in the previous studies.

2.3 Computation of pressure

By taking divergence of the Navier-Stokes equations, following Poisson equation is derived for the pressure fields:

$$\nabla^2 p = -\frac{\partial u_i}{\partial x_j}\frac{\partial u_j}{\partial x_i}, \qquad \left.\frac{\partial p}{\partial y}\right|_{wall} = \frac{1}{Re_\tau}\frac{\partial^2 v}{\partial y^2}, \tag{2.2}$$

where p is pressure and flow variables are normalized with the wall-shear velocity u_τ and the channel half-height h. To compute the pressure, the Poisson equation

is solved by a Fourier/Chebychev-tau method as described in Kim *et al.* (1987) and Kim (1989).

The source terms in the Poisson equation is sometimes divided into rapid and slow parts by taking Reynolds decompositions to the velocity field (Kim, 1989):

$$\nabla^2 p_r = -2\frac{\mathrm{d}U}{\mathrm{d}y}\frac{\partial v'}{\partial x}, \qquad \left.\frac{\partial p_r}{\partial y}\right|_{wall} = 0, \tag{2.3a}$$

$$\nabla^2 p_s = -\frac{\partial u_i'}{\partial x_j}\frac{\partial u_j'}{\partial x_i}, \qquad \left.\frac{\partial p_s}{\partial y}\right|_{wall} = 0, \tag{2.3b}$$

where U is the mean streamwise velocity, $u_1'(=u')$, $u_2'(=v')$ and $u_3'(=w')$ are x, y and z components of the fluctuating velocity and the subscript r and s indicate rapid and slow, respectively. Here, the source term of rapid pressure indicates linear interaction of the velocity fluctuation with mean shear $\mathrm{d}U/\mathrm{d}y$, while that of slow pressure denotes nonlinear interactions between the velocity fluctuations. In this respect, rapid and slow pressure are also referred to as linear and nonlinear pressure, respectively (Kim, 1989). Note that both equations (2.3a) and (2.3b) have homogeneous Neumann boundary conditions, but the actual boundary condition for pressure is inhomogeneous, as shown in equation (2.2). The effect of inhomogeneous boundary condition goes to the stokes pressure as follows (Mansour *et al.*, 1988):

$$\nabla^2 p_{st} = 0, \qquad \left.\frac{\partial p_{st}}{\partial y}\right|_{wall} = \frac{1}{Re_\tau}\frac{\partial^2 v'}{\partial y^2}, \tag{2.4}$$

where the subscript *st* indicates stokes pressure. However, in the turbulent channel flow, it has been shown that the role of stokes pressure is negligible (Kim, 1989; Jiménez & Hoyas, 2008). Therefore, the rest of this paper is concerned only with rapid and slow pressure.

It should be noted that in the case of LES, equation (2.2) becomes:

$$\nabla^2\tilde{p} = -\frac{\partial\tilde{u}_i}{\partial x_j}\frac{\partial\tilde{u}_j}{\partial x_i} - \frac{\partial}{\partial x_i}\left(\frac{\partial\tau_{ij}}{\partial x_j}\right), \qquad \left.\frac{\partial\tilde{p}}{\partial y}\right|_{wall} = \frac{1}{Re_\tau}\frac{\partial^2\tilde{v}}{\partial y^2}, \tag{2.5}$$

where $\tau_{ij} = \widetilde{u_i u_j} - \tilde{u}_i\tilde{u}_j$ is SGS stress and $\tilde{\cdot}$ denotes filtered variables. Comparing equations (2.5) and (2.2), an additional source term emerges from the SGS stress term. Figure 2.2 illustrates the effect of the additional source term for the highest C_s case (i.e. $L1600c$ in table 2.1). As shown, regardless of the SGS term, premultiplied one-dimensional spectra of pressure fluctuations are almost identical. Therefore, pressure, rapid pressure and slow pressure in this study are computed by solving equations (2.2), (2.3a) and (2.3b), respectively, with filtered velocity components. To avoid confusion, pressure derived from the equation (2.2) is referred to as a full pressure (p_f) in the below.

2.4 Preliminary test

For the purpose of confirming that the present numerical experiments start from reliable statistics, results of the reference simulation ($F1600$ in table 2.1) are compared with those of previous DNS study by Hoyas & Jiménez (2006). Figure 2.3 shows root-mean-square velocity and pressure fluctuations. The statistics from $F1600$ show reasonable agreement with those of previous DNS. In particular, the results of rapid pressure fluctuations from $F1600$ agree much better with DNS, compared to those of full or slow pressure fluctuations. This is merely because the unresolved part from LES comes from nonlinear interactions (i.e. p_f and p_s). Also, premultiplied one-dimensional streamwise and spanwise spectra of the full pressure fluctuations obtained from case $F1600$ are shown in figure 2.4. Here, dashed lines aligned with spectra indicate that the

streamwise and spanwise length scales at the logarithmic layer are linearly proportional to the distance from the wall. It has been shown in previous studies that the spanwise length scale of energy-containing motions grows linearly with the distance from the wall (Tomkins & Adrian, 2003; del Álamo *et al.*, 2004; Hutchins *et al.*, 2005; Hwang, 2015), and the streamwise length scale has a bimodal spectral distribution at every wall-normal location. Therefore, Hwang (2015) isolated attached eddies based on a given spanwise length scale. In this respect, the spanwise length scale is selected as a characteristic length scale for consistency. The premultiplied one-dimensional spectra of rapid and slow pressure fluctuations are given in figures 2.5 and 2.6, and the linear scaling is also clearly shown. This result is consistent with the previous study by Jiménez & Hoyas (2008), showing the logarithmic behavior of mean-square rapid and slow pressure fluctuations in terms of wall-normal location.

Then, it has been verified that the current filtering technique in equation (2.1) provides the consistent results as in Hwang (2015). Normalized second-order statistics of self-sustaining attached eddies are shown in figure 2.7. All of the attached eddies in the logarithmic region show self-similarity below certain wall-normal locations, with respect to their given spanwise length scale. It should be noted that the non-self-similar part originates from the motions larger than the given spanwise length scale, which is removed in each of the simulations (see Hwang (2013, 2015) for a detailed explanation). Therefore, as current numerical experiments exhibit consistent results with previous studies (Hwang, 2013, 2015), pressure fluctuations of self-sustaining attached eddies are analyzed in the following chapter.

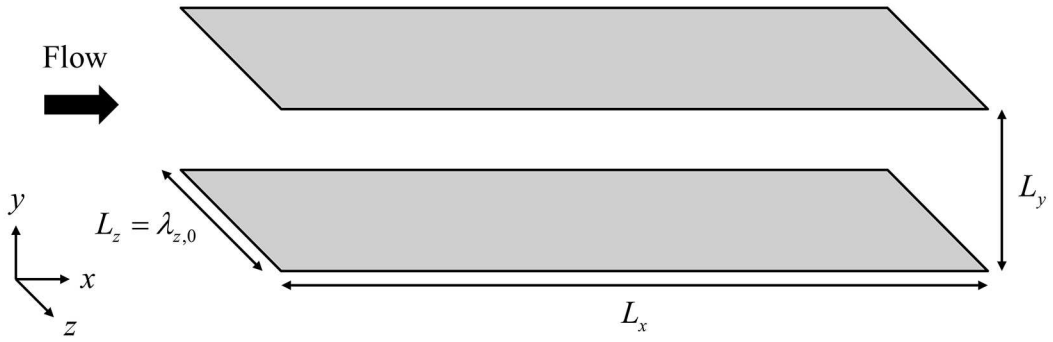

Figure 2.1. Three-dimensional view of the computational domain.

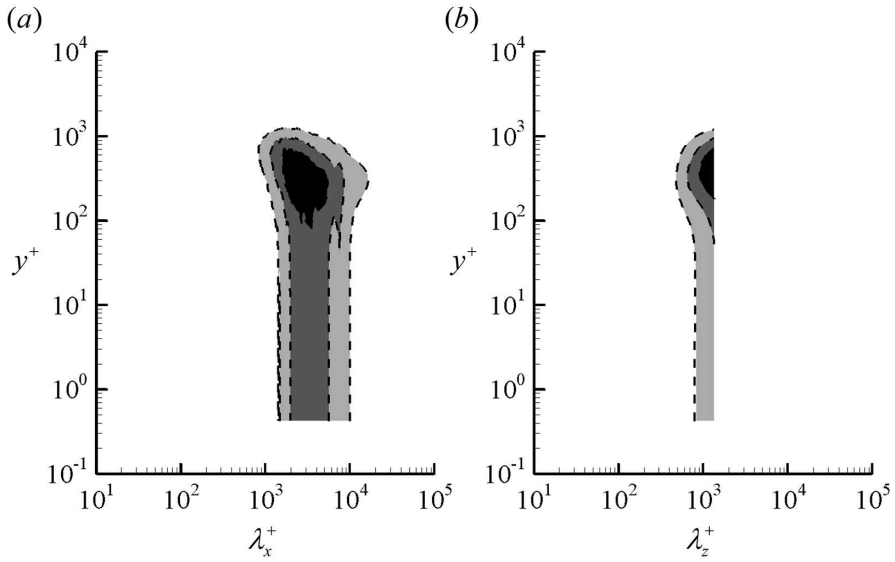

Figure 2.2. Premultiplied one-dimensional (a) streamwise and (b) spanwise spectra of pressure fluctuations for $L1600c$. Here, the dashed and shaded contours indicate spectra with and without the SGS term, respectively, and the contour levels are chosen as 0.25, 0.5 and 0.75 times each of the maximum.

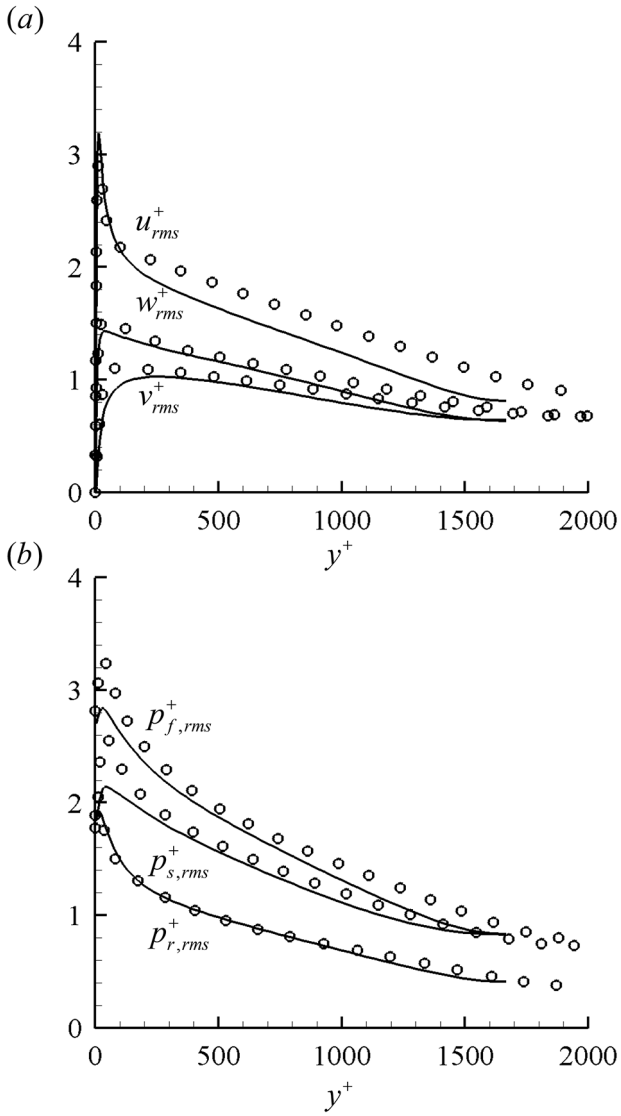

Figure 2.3. Root-mean-square (a) velocity and (b) pressure fluctuations of the reference simulations: ——, $F1600$; ∘, DNS at $Re_\tau = 2000$ (Hoyas & Jiménez, 2006).

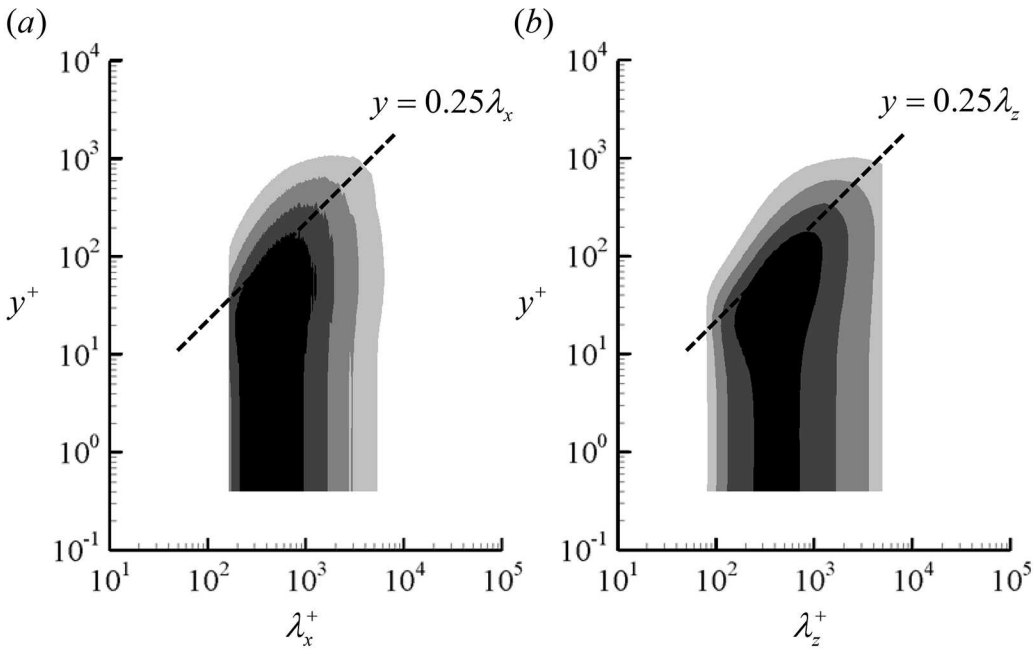

Figure 2.4. Premultiplied one-dimensional (a) streamwise and (b) spanwise spectra of full pressure fluctuations ($F1600$). The contour levels are chosen as 0.2, 0.4, 0.6 and 0.8 times each of the maximum.

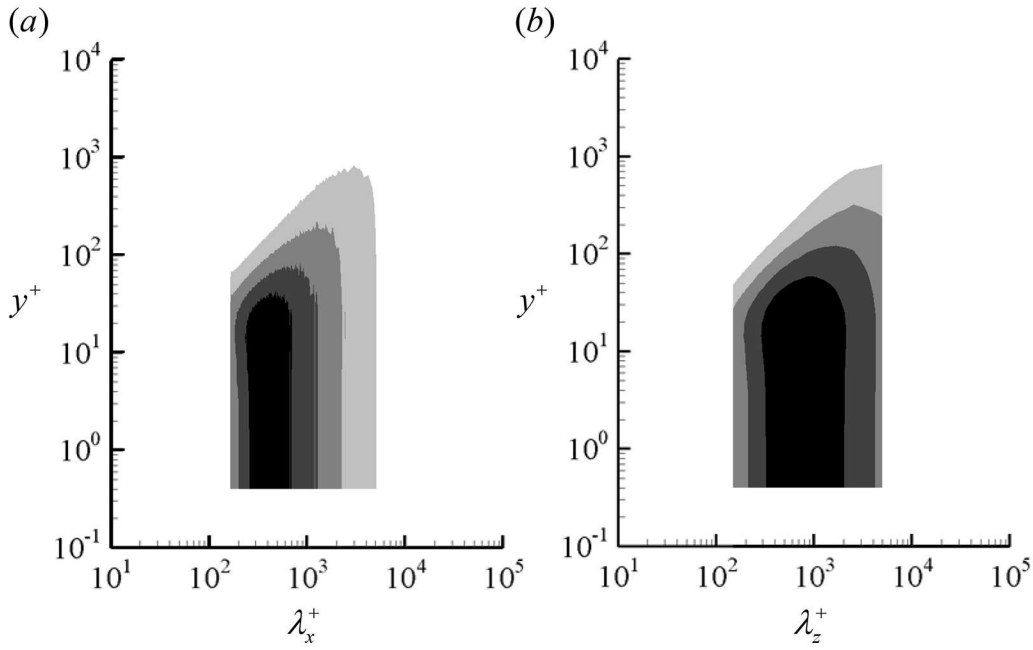

Figure 2.5. Premultiplied one-dimensional (a) streamwise and (b) spanwise spectra of rapid pressure fluctuations ($F1600$). The contour levels are chosen as 0.2, 0.4, 0.6 and 0.8 times each of the maximum.

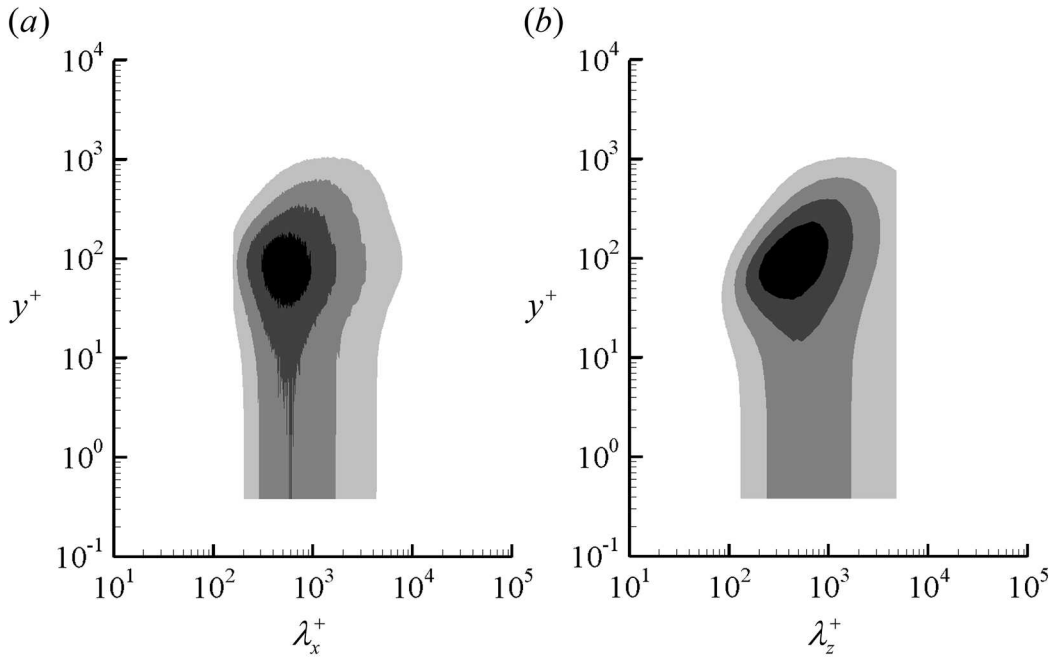

Figure 2.6. Premultiplied one-dimensional (a) streamwise and (b) spanwise spectra of slow pressure fluctuations ($F1600$). The contour levels are chosen as 0.2, 0.4, 0.6 and 0.8 times each of the maximum.

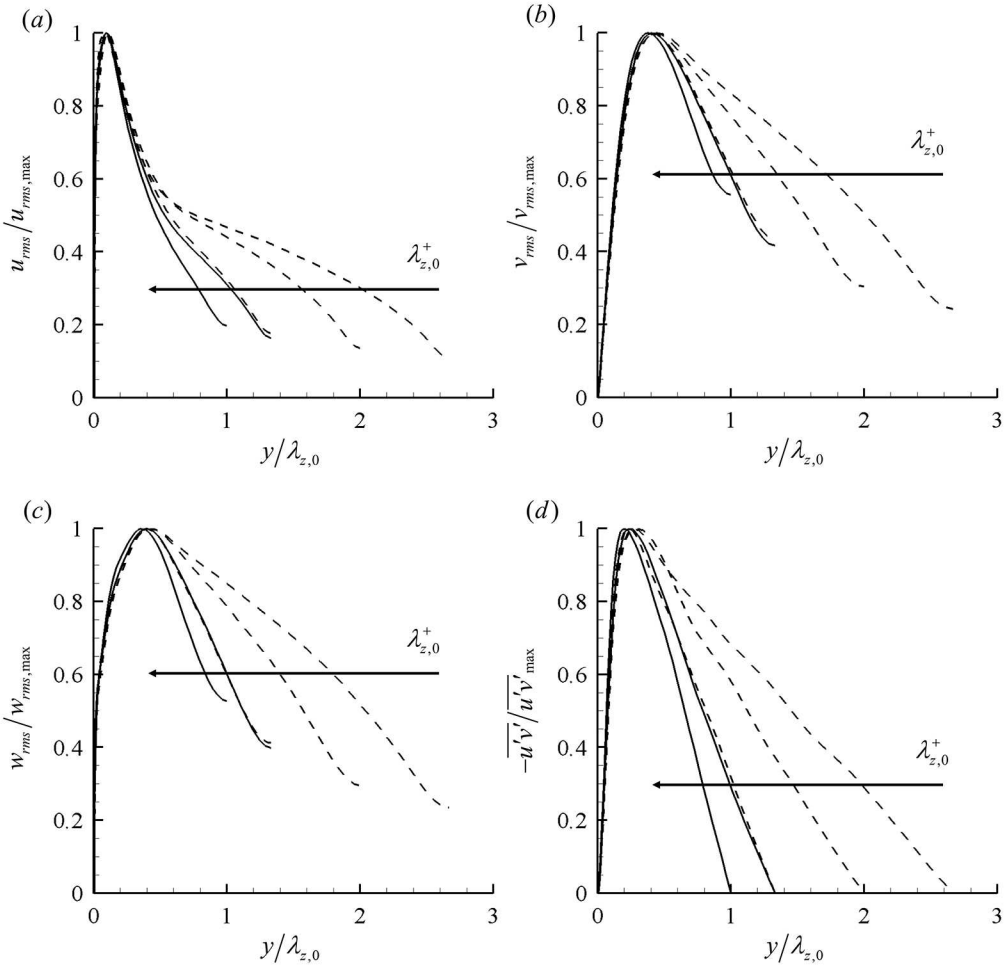

Figure 2.7. Normalized second-order statistics of (a) streamwise, (b) wall-normal, (c) spanwise velocities and (d) Reynolds stress: ——, $L900a, b$; - - -, $L1600a, b, c$.

Chapter 3

Pressure fluctuations of self-sustaining attached eddies

3.1 Self-similarity of attached eddies

Figures 3.1, 3.2 and 3.3 show normalized second-order statistics of full, rapid and slow pressure fluctuations, respectively. The vertical axis is normalized by the maximum value of each attached eddy, and the horizontal axis is normalized by the given spanwise length scale $\lambda_{z,0}$. It is shown that statistics from attached eddies of several different spanwise sizes at two different Reynolds numbers collapse very well below $y \lesssim 0.25\lambda_{z,0}$, indicating that all of the pressure statistics are self-similar with respect to $\lambda_{z,0}$. Note that this is consistent with the velocity statistics (Hwang, 2015). Also, as was observed in the previous studies (Hwang, 2013, 2015), non-self-similar part occurs above $0.25\lambda_{z,0}$, originates from the removed motions at $\lambda_z > \lambda_{z,0}$.

Premultiplied one-dimensional streamwise spectra of full, rapid, and slow pressure fluctuations are illustrated in figures 3.4, 3.5 and 3.6, respectively. Peak locations in the spectra are self-similar with $\lambda_{z,0}$, also consistent with the velocity statistics (Hwang, 2015), showing that structures of the pressure fluctuations of each attached eddy is statistically self-similar with its spanwise size. The peak location of full pressure fluctuations spectra in figure 3.4 is located at

$\lambda_x \simeq 2\lambda_{z,0}$ and $y \simeq 0.25\lambda_{z,0}$. This is consistent with the peak location in figure 3.1, as well as the linear scaling in figure 2.4. It is notable that the spectra of rapid pressure fluctuations have large value in the region close to the wall (unlike slow pressure fluctuations), which is due to large near-wall $\mathrm{d}U/\mathrm{d}y$ in the source term (see equation (2.3a)). This is also indicated in figure 3.2, showing $p_{r,rms} \simeq p_{r,rms,\max}$ in the region of $y \lesssim 0.1\lambda_{z,0}$. To compare the spectra of pressure fluctuations with those of velocity fluctuations, figures 3.7, 3.8 and 3.9 are shown. As observed in the previous study of Hwang (2015), these spectra represent that the attached eddies are composed of two interconnected structures: a long streaky structure which mainly carries streamwise turbulent kinetic energy ($\lambda_x \simeq 10\lambda_{z,0}$ and $y \simeq 0.1\lambda_{z,0}$) in figure 3.7 and a short and tall vortical structure carrying all the fluctuating velocity components ($\lambda_x \simeq 2\lambda_{z,0}$ and $y \simeq 0.5\lambda_{z,0}$) in figures 3.8 and 3.9. Note that these figures are consistent with those in Hwang (2015). On the other hand, the maximum value in the spectra of full pressure fluctuations is located at $\lambda_x \simeq 2\lambda_{z,0}$ and $y \simeq 0.25\lambda_{z,0}$ (see figure 3.4). The peak location of λ_x is similar to that of v' and w' spectra (streamwise vortical structures). Also, the peak location of y is in between that of u' ($y \simeq 0.1\lambda_{z,0}$) and v' or w' ($y \simeq 0.5\lambda_{z,0}$) spectra. Figure 3.10 indicates the instantaneous field of $L1600c$. The bimodal characteristics described above are well represented in figure 3.10 (a). Long meandering streaky motions reach down to the wall, and streamwise vortical structures are aligned to that. In addition, isosurfaces of full pressure fluctuations are added in figure 3.10 (b), showing comparable streamwise length scale with that of streamwise vortical structures and wall-normal location between long streaky motions and streamwise vortical structures. Note that all of the attached eddies exhibit qualitatively the same behavior, as was observed in the previous study (Hwang, 2015).

3.2 Time correlation functions

So far, the statistical behavior of pressure fluctuations of attached eddies has been analyzed. To explore the dynamical features, we consider minimal unit simulations in this section. Table 3.1 summarizes simulation parameters for self-sustaining minimal attached eddies. ML in the case name indicates minimal attached eddy in the log layer and T is averaging time. It has been shown in Hwang & Cossu (2010) and Hwang & Bengana (2016) that the smallest computational domain size which contains the self-sustaining attached eddies at the given spanwise length scale $\lambda_{z,0}$ (i.e. the minimal unit) is:

$$L_z = \lambda_{z,0}, L_x = 2L_z, \tag{3.1}$$

where L_x and L_z correspond to the streamwise and spanwise domain size, respectively. In this regard, all simulations in table 3.1 have this ratio of computational domain size, as shown in figure 3.11. Note that the use of the minimal unit has been verified to have little effect on second-order statistics of attached eddies, compared with the results from a long streamwise domain as in table 2.1 (Hwang & Bengana, 2016). To ensure that time correlation functions given below are fully converged, a sufficient time interval is used for averaging.

As briefly mentioned in the introduction, it has been shown that the attached eddies at all scales are composed of long streaky motions and quasi-streamwise vortical structures, and they undergo the self-sustaining process (Hamilton *et al.*, 1995; Schoppa & Hussain, 2002; Hwang, 2015; Hwang & Bengana, 2016): streaks are amplified by streamwise vortices via the linear lift-up effect and these streaks meander due to streak instability and/or transient growth, which induce the regeneration of streamwise vortices by nonlinear pro-

Case	Re_m	Re_τ	L_x/h	L_z/h	$N_x \times N_y \times N_z$	C_s	Tu_τ/h
$ML900a$	38133	890	1.5	0.75	24×91×24	0.2	311
$ML900b$	38133	922	2	1	32×91×32	0.25	322
$ML1600a$	73333	1448	0.75	0.375	24×145×24	0.2	132
$ML1600b$	73333	1580	1	0.5	32×145×32	0.3	144
$ML1600c$	73333	1750	1.5	0.75	48×145×48	0.4	159

Table 3.1. Simulation parameters for self-sustaining minimal attached eddies.

cess. In Hwang & Bengana (2016), this time sequence was analyzed from the time correlation functions defined as follows:

$$C_{ij}(\tau) = \frac{\langle E_i(t+\tau) E_j(t) \rangle}{\sqrt{\langle E_i^2(t) \rangle \langle E_j^2(t) \rangle}}, \tag{3.2}$$

where E_i or E_j is energy variable and $\langle \cdot \rangle$ denotes time average. It was verified that the temporal evolution of streaks can be well characterized by following variables E_u or E_0:

$$E_u = \frac{1}{2V_h} \int_{\Omega_h} (u')^2 \, dV, \tag{3.3a}$$

$$E_0 = \int_{\Omega_{y,h}} \left(\left| \hat{u'} \right|^2 + \left| \hat{v'} \right|^2 + \left| \hat{w'} \right|^2 \right)_{y;k_x=0,k_z=2\pi/L_z} dy, \tag{3.3b}$$

where Ω_h is the computational domain of $[0, L_x]$ in the streamwise direction, $[0, 2/3\lambda_{z,0}]$ (lower) or $[L_y, L_y - 2/3\lambda_{z,0}]$ (upper) for the wall-normal direction and $[0, L_z]$ for the spanwise direction. V_h is volume of Ω_h and $\Omega_{y,h}$ is lower or upper part of the wall-normal domain of Ω_h. Note that $2/3\lambda_{z,0}$ is determined as the integral span in y-direction, because in the case of the largest attached

eddies (large-scale and very-large-scale motions), $2/3\lambda_{z,0}$ becomes channel half height h as $\lambda_{z,0} = 1.5h$ (Hwang & Bengana, 2016). As a streaky motion can be characterized as a long structure in streamwise direction (i.e. $k_x = 0$) containing most of the streamwise turbulent kinetic energy, both E_u and E_0 capture the temporal evolution of streaks well. Figure 3.12 (a) shows that E_u and E_0 are strongly correlated to each other, as verified in Hwang & Bengana (2016). On the other hand, quasi-streamwise vortical structures were well tracked by E_v or E_w, as streaks contain very little turbulent kinetic energy in the wall-normal and spanwise directions:

$$E_v = \frac{1}{2V_h} \int_{\Omega_h} (v')^2 \, dV, \tag{3.4a}$$

$$E_w = \frac{1}{2V_h} \int_{\Omega_h} (w')^2 \, dV. \tag{3.4b}$$

E_v and E_w also showed strong correlation such that $C_{vw}(\tau = 0) \simeq 0.6$ (see figure 3.12 (b)), consistent with Hwang & Bengana (2016). Lastly, streamwise meandering streaks were well described by following variable E_1, as it computes the energy of the smallest wavenumber components:

$$E_1 = \int_{\Omega_{y,h}} \left(\left|\hat{u'}\right|^2 + \left|\hat{v'}\right|^2 + \left|\hat{w'}\right|^2 \right)_{y;k_x=2\pi/L_x,k_z=2\pi/L_z} dy. \tag{3.5}$$

Consequently, E_u (or E_0), E_1 and E_v (or E_w) capture the temporal behavior of streaks, streamwise meandering streaks and streamwise vortices, respectively, and these three components constitute the self-sustaining process (see Hwang & Bengana (2016) for further details).

Likewise, two additional variables E_{p_r} and E_{p_s} are defined for the rapid and

slow pressure fluctuations, respectively, to analyze their dynamics:

$$E_{p_r} = \frac{1}{2V_h} \int_{\Omega_h} \left(p_r'\right)^2 dV, \tag{3.6a}$$

$$E_{p_s} = \frac{1}{2V_h} \int_{\Omega_h} \left(p_s'\right)^2 dV. \tag{3.6b}$$

Then, time correlation functions defined as equation (3.2) are computed to figure out what process amplifies either rapid or slow pressure fluctuations in the self-sustaining cycle.

Computed correlation functions are shown in figure 3.13 and 3.14. Figure 3.13 (a) shows cross-correlation functions between E_{p_r} and E_{p_s}, showing that E_{p_r} and E_{p_s} are strongly correlated to each other. This implies that both rapid and slow pressure fluctuations are amplified almost simultaneously. The cross correlation functions of $i = u$ and $j = p_r, p_s$ are given in figure 3.13 (b). From the phase difference, the time sequence of processes can be figured out: E_u statistically reaches its extremum $\Delta\tau u_\tau/\lambda_{z,0} \simeq 0.5$ before E_{p_r} and E_{p_s} reaches their extremum. The corresponding time sequence is E_u to $E_{p_r}\&E_{p_s}$. Similarly from figure 3.14 (a), where $i = v$ and $j = p_r, p_s$ are illustrated, E_v reaches its extremum $\Delta\tau u_\tau/\lambda_{z,0} \simeq 0.2$ after E_{p_r} and E_{p_s} reaches their extremum. Accordingly, the time sequence is E_u to $E_{p_r}\&E_{p_s}$ to E_v, indicating that streaks (E_u) occur first, rapid and slow pressure fluctuations ($E_{p_r}\&E_{p_s}$) follow, then streamwise vortices (E_v) are amplified and they again induces streaks. Lastly, figure 3.14 (b) clearly shows that E_1 is very well correlated to $E_{p_r}\&E_{p_s}$, implying that the meandering motion of the streaks is an important feeding mechanism of pressure fluctuations. Therefore, the final time sequence is:

$$E_u \rightarrow E_{p_r}\&E_{p_s}\&E_1 \rightarrow E_v. \tag{3.7}$$

In other words, both rapid and slow pressure fluctuations are amplified together with the meandering motion of the streaks. One may think that $\Delta\tau u_\tau/\lambda_{z,0}$ appearing in C_{up_r} and C_{up_s} in figure 3.13 (b) are different. However, in practice, the difference of $\Delta\tau u_\tau/\lambda_{z,0}$ between E_{p_r} and E_{p_s} is too small, which makes it very difficult to distinguish which one comes first. Also, it should be noted that the correlation value of C_{up_r} itself is not so large (the minimum of the correlation values shown in figures 3.13 and 3.14), indicating that $\Delta\tau u_\tau/\lambda_{z,0}$ from C_{up_r} would be less reliable than others. Another important thing is that all the correlation functions scale fairly well with $\lambda_{z,0}$, suggesting that the pressure field of each attached eddy is also dynamically self-similar with respect to its spanwise size $\lambda_{z,0}$, consistent with the velocity fluctuations (Hwang & Bengana, 2016).

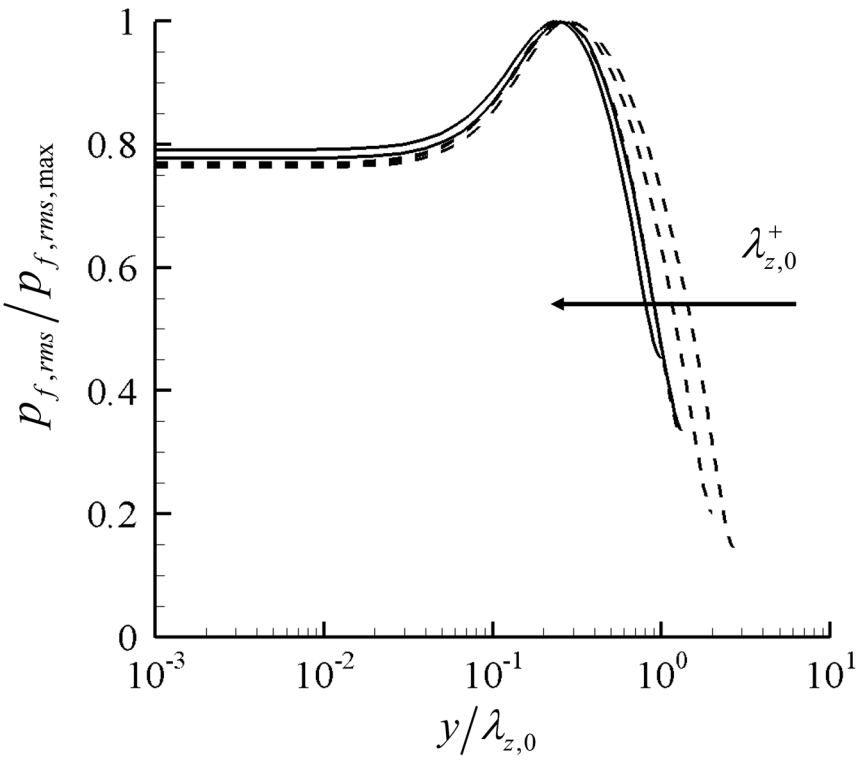

Figure 3.1. Normalized second-order statistics of full pressure fluctuations: ——, $L900a, b$; - - -, $L1600a, b, c$.

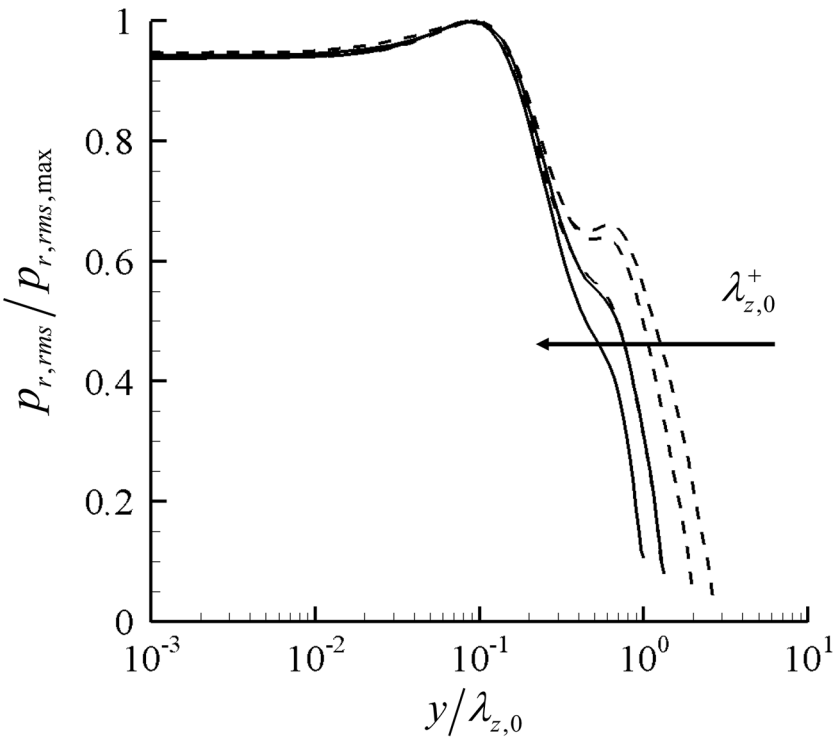

Figure 3.2. Normalized second-order statistics of rapid pressure fluctuations: ——, $L900a, b$; - - -, $L1600a, b, c$.

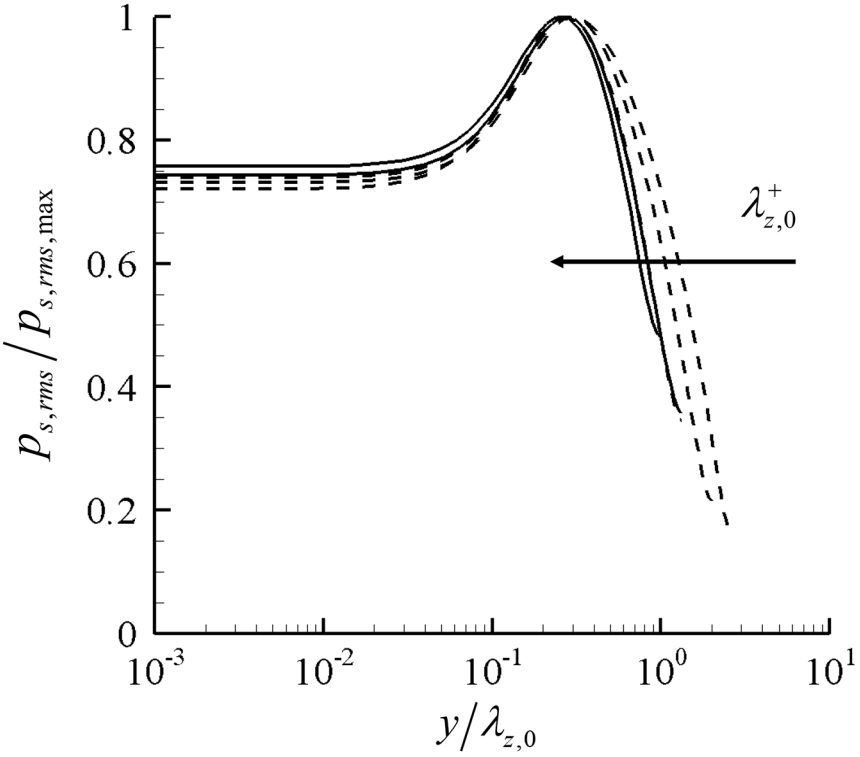

Figure 3.3. Normalized second-order statistics of slow pressure fluctuations: ——, $L900a, b$; - - -, $L1600a, b, c$.

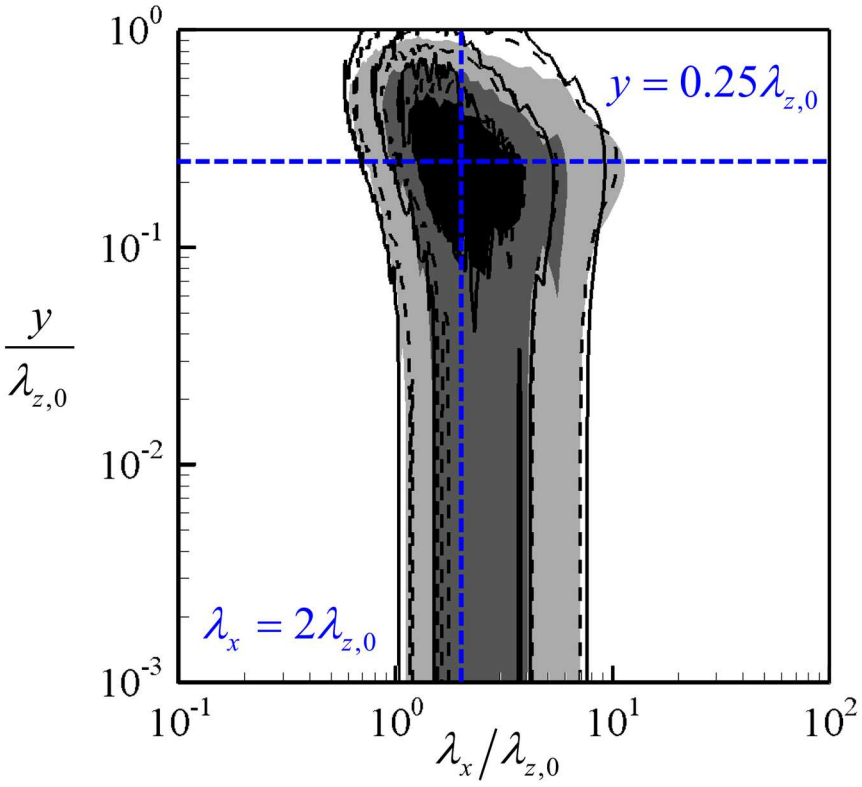

Figure 3.4. Premultiplied one-dimensional streamwise spectra of full pressure fluctuations. Here, the solid, dashed and shaded contours indicate $L1600a$, $L1600b$ and $L1600c$, respectively, and the contour levels are chosen as 0.25, 0.5 and 0.75 times each of the maximum.

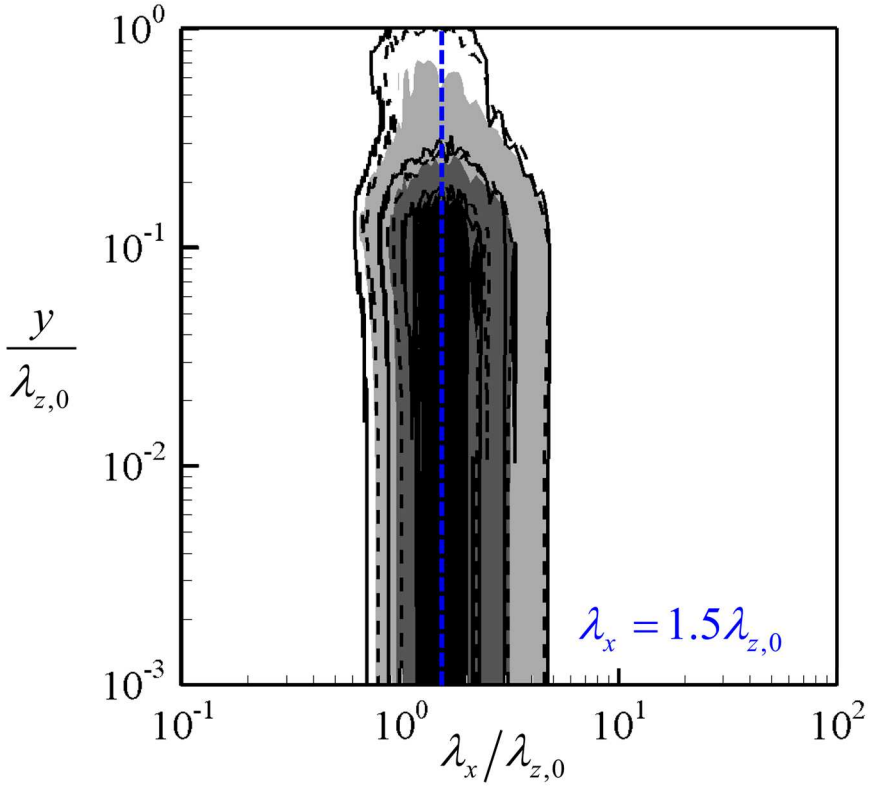

Figure 3.5. Premultiplied one-dimensional streamwise spectra of rapid pressure fluctuations. Here, the solid, dashed and shaded contours indicate $L1600a$, $L1600b$ and $L1600c$, respectively, and the contour levels are chosen as 0.25, 0.5 and 0.75 times each of the maximum.

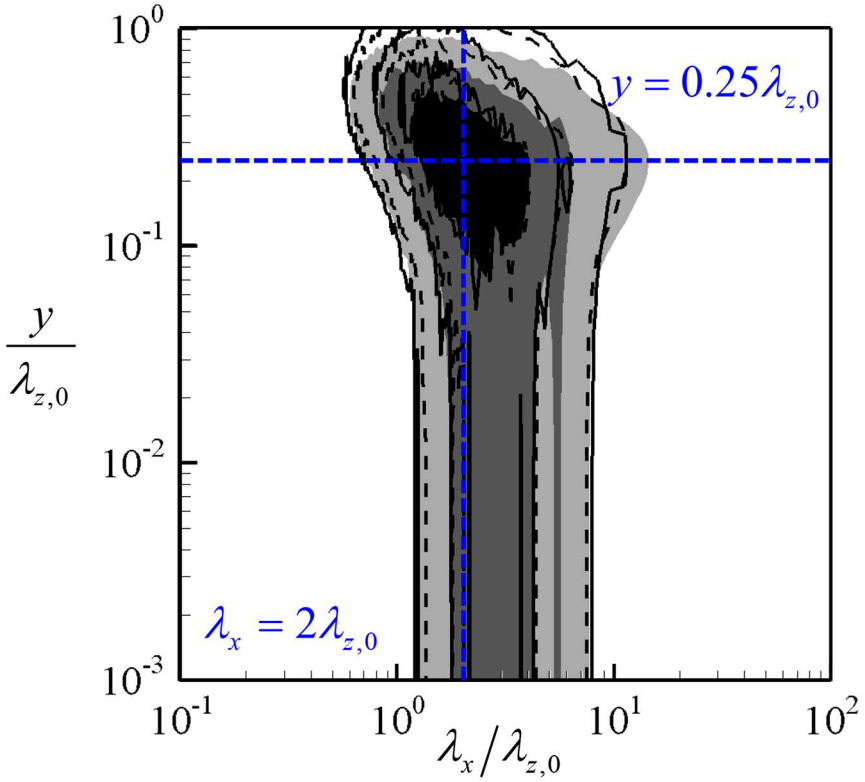

Figure 3.6. Premultiplied one-dimensional streamwise spectra of slow pressure fluctuations. Here, the solid, dashed and shaded contours indicate $L1600a$, $L1600b$ and $L1600c$, respectively, and the contour levels are chosen as 0.25, 0.5 and 0.75 times each of the maximum.

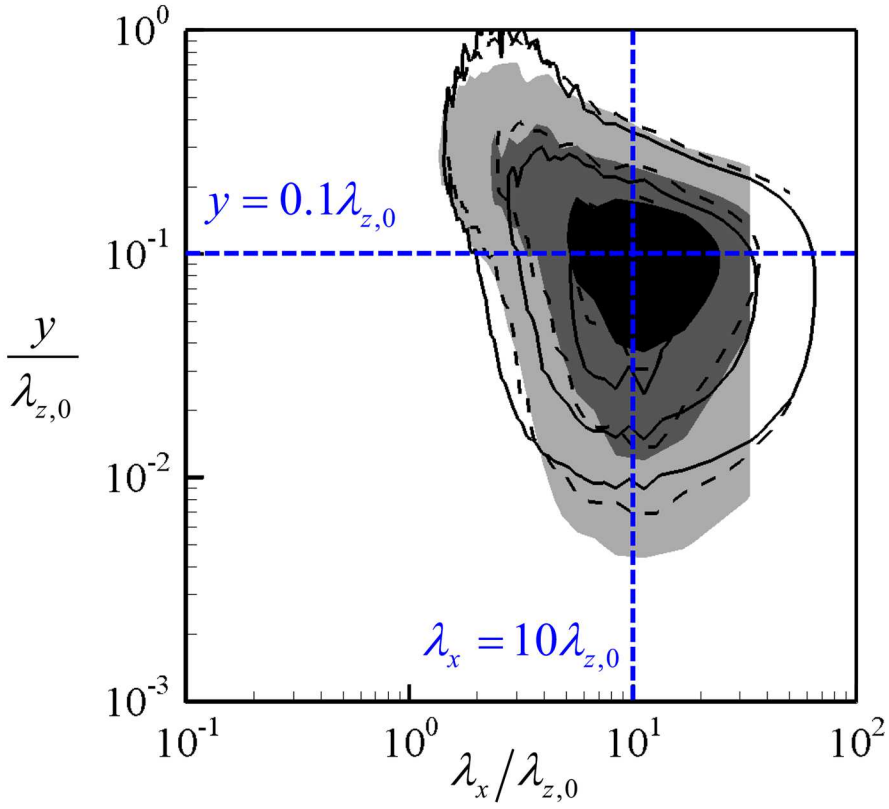

Figure 3.7. Premultiplied one-dimensional streamwise spectra of streamwise velocity fluctuations. Here, the solid, dashed and shaded contours indicate $L1600a$, $L1600b$ and $L1600c$, respectively, and the contour levels are chosen as 0.25, 0.5 and 0.75 times each of the maximum.

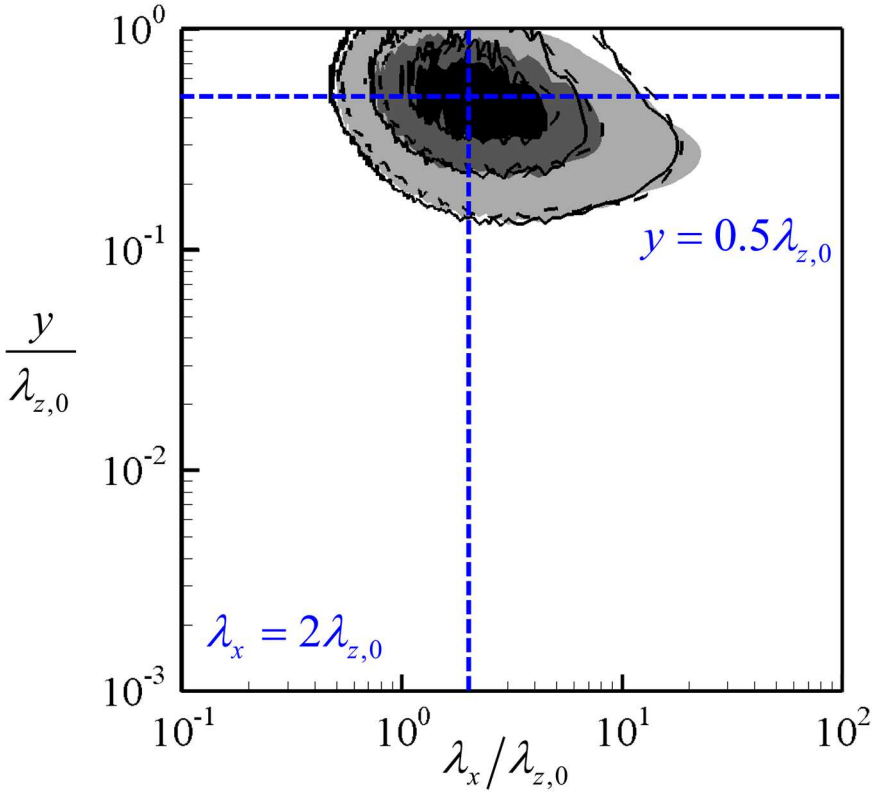

Figure 3.8. Premultiplied one-dimensional streamwise spectra of wall-normal velocity fluctuations. Here, the solid, dashed and shaded contours indicate $L1600a$, $L1600b$ and $L1600c$, respectively, and the contour levels are chosen as 0.25, 0.5 and 0.75 times each of the maximum.

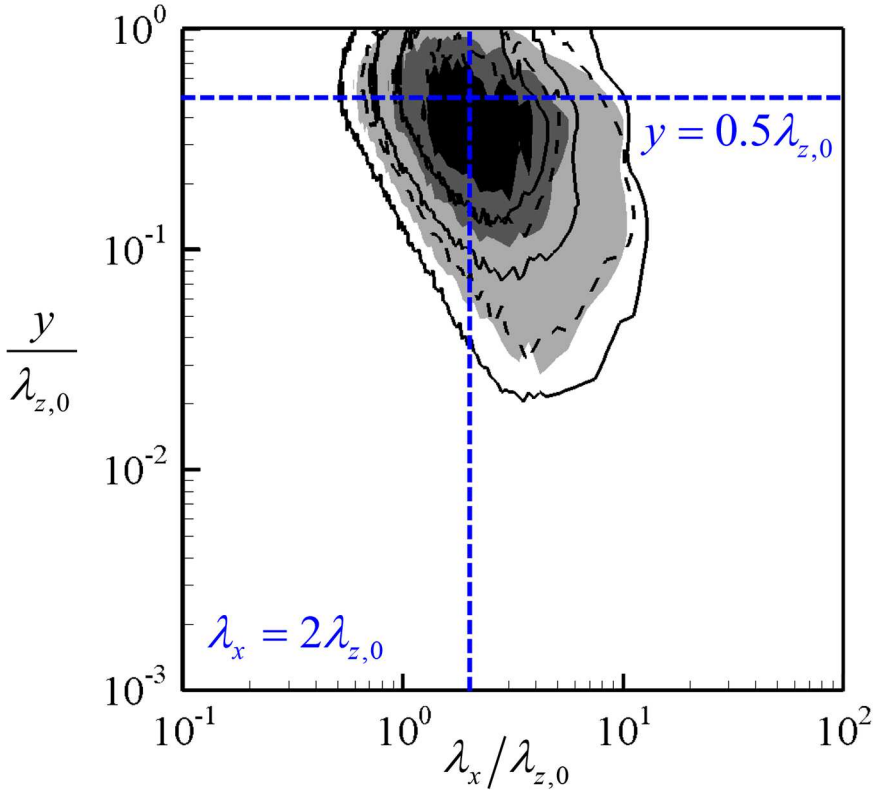

Figure 3.9. Premultiplied one-dimensional streamwise spectra of spanwise velocity fluctuations. Here, the solid, dashed and shaded contours indicate $L1600a$, $L1600b$ and $L1600c$, respectively, and the contour levels are chosen as 0.25, 0.5 and 0.75 times each of the maximum.

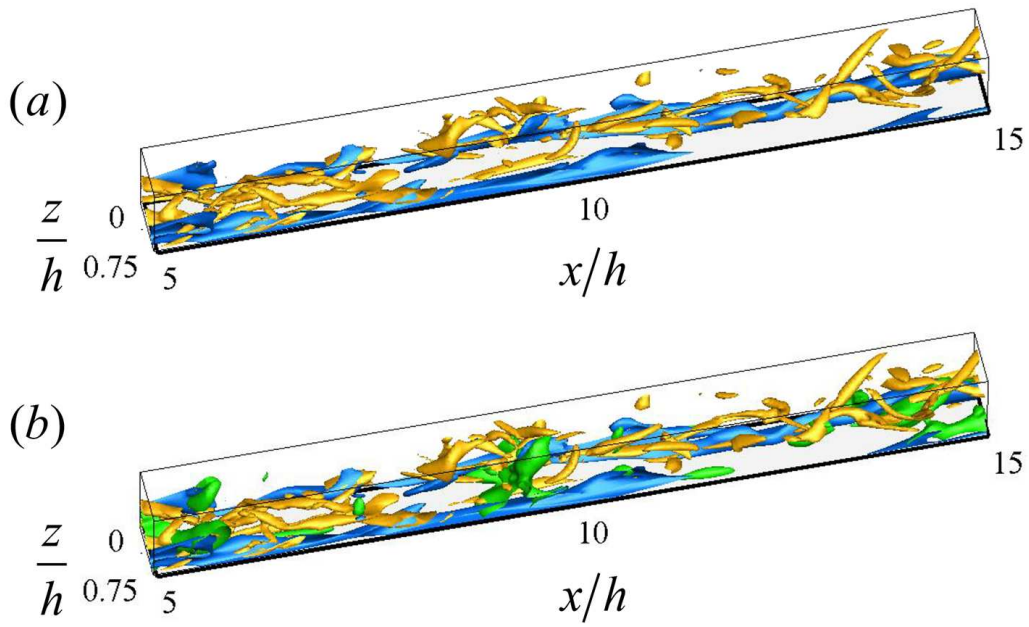

Figure 3.10. Instantaneous flow field of $L1600c$: (a) long streaky motions (blue isosurfaces of $u'^{+} = -2.5$) and streamwise vortical structures (yellow isosurfaces of $Q = 1.1 \times 10^{-4} u_\tau^4/\nu^2$, where Q is the second invariant of the velocity gradient tensor); (b) green isosurfaces of $p_f'^{+} = -2.5$ is added to (a).

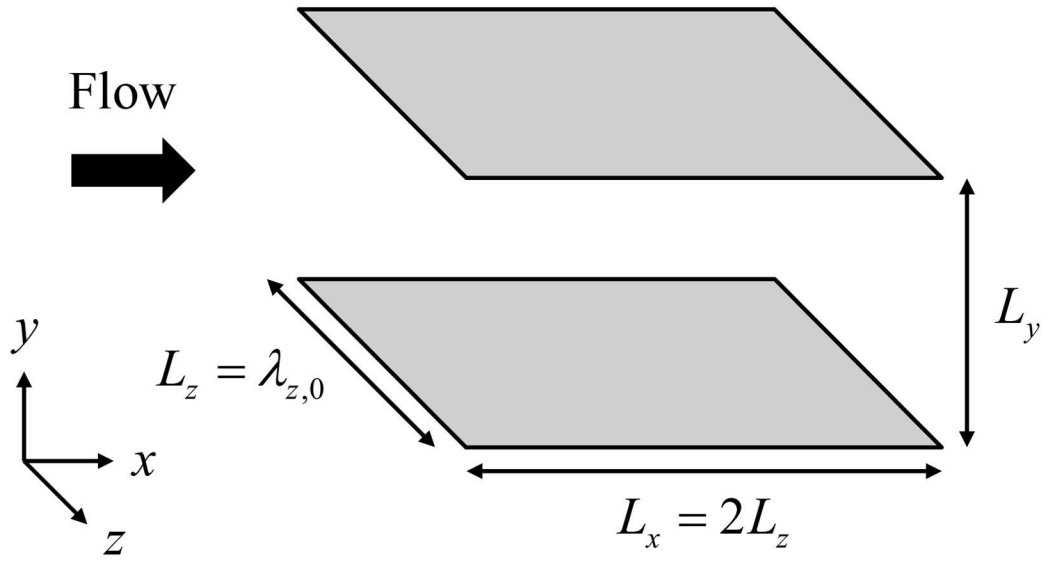

Figure 3.11. Three-dimensional view of the computational domain for minimal attached eddies.

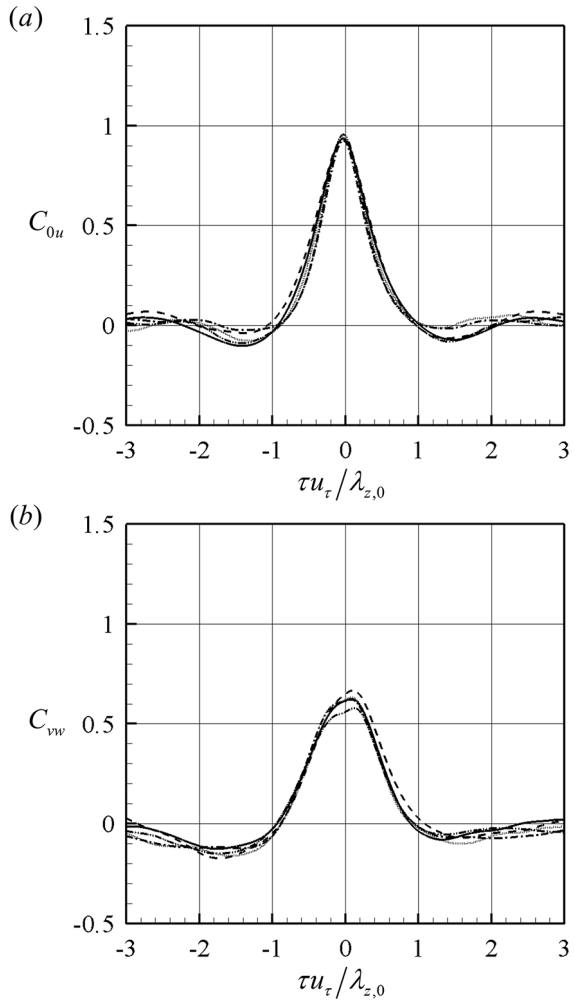

Figure 3.12. Cross-correlation functions of (*a*) $C_{0u}(\tau)$ and (*b*) $C_{vw}(\tau)$: ——, $ML900a$; - - - -, $ML900b$; — · —, $ML1600a$; — ·· —, $ML1600b$; · · · · ·, $ML1600c$.

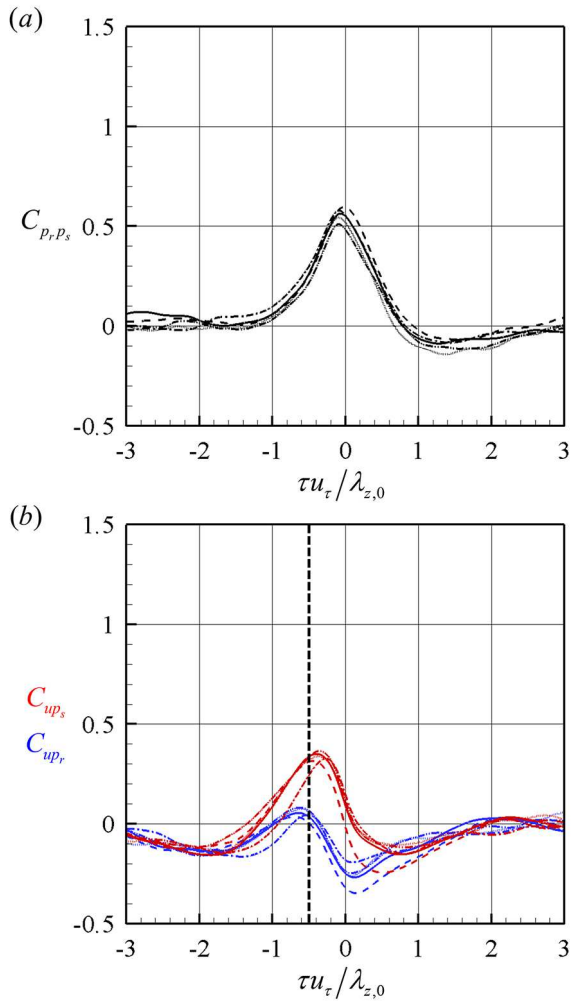

Figure 3.13. Cross-correlation functions of (*a*) $C_{p_r p_s}(\tau)$ and (*b*) $C_{up_r}(\tau)$ (blue) and $C_{up_s}(\tau)$ (red): ——, $ML900a$; - - - -, $ML900b$; — · —, $ML1600a$; — · ·—, $ML1600b$; · · · · ·, $ML1600c$.

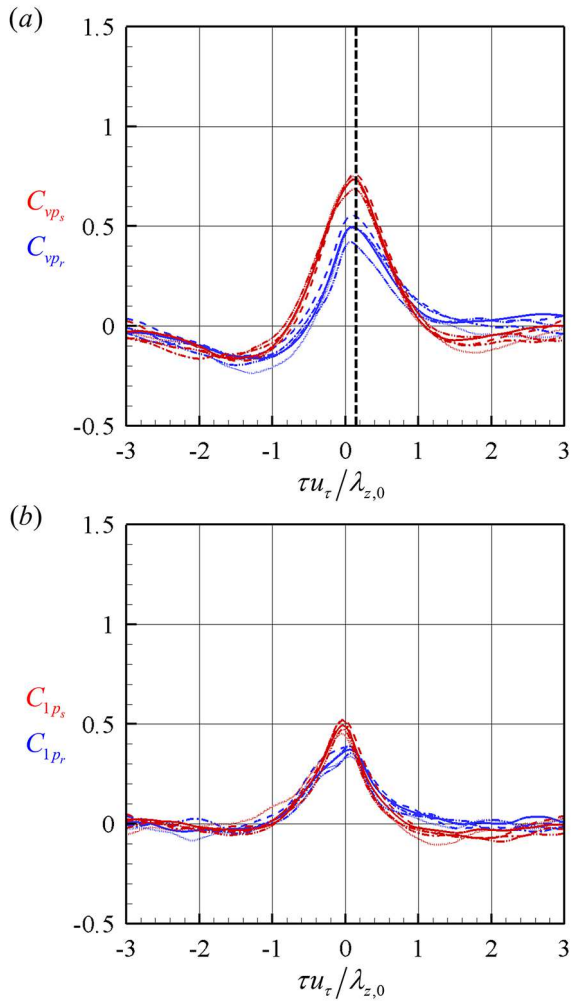

Figure 3.14. Cross-correlation functions of (*a*) $C_{vp_r}(\tau)$ (blue) and $C_{vp_s}(\tau)$ (red) and (*b*) $C_{1p_r}(\tau)$ (blue) and $C_{1p_s}(\tau)$ (red): ——, $ML900a$; - - - -, $ML900b$; — · —, $ML1600a$; — · · —, $ML1600b$; · · · · ·, $ML1600c$.

Chapter 4

Discussion

4.1 Pressure amplification process and attached eddies

It has been shown that the pressure fluctuations of self-sustaining attached eddies are both statistically (in section 3.1) and dynamically (in section 3.2) self-similar with respect to each of their spanwise size. Self-similarity of the attached eddies with Neumann boundary condition of pressure would theoretically give logarithmic dependence of pressure fluctuations and k_x^{-1} spectra according to Townsend's hypothesis (Townsend, 1976; Perry & Chong, 1982; Perry & Marusic, 1995; Nickels *et al.*, 2005; Hwang, 2015). It should be mentioned that as Townsend's attached eddy hypothesis was built on the assumption of slip boundary conditions (Townsend, 1976), the pressure is an ideal candidate for analyzing his hypothesis due to slip of pressure at the wall. Note that pressure fluctuations in the near-wall region are strong at all length scales due to Neumann boundary conditions (see figure 2.4). Also, evidence for theoretical predictions based on Townsend's hypothesis have been recently provided. Tsuji *et al.* (2007) and Klewicki *et al.* (2008) have found the k_x^{-1} spectra at high Reynolds number turbulent boundary layer flow, and the logarithmic wall-normal dependence of pressure fluctuations including rapid and slow parts have been reported by Jiménez & Hoyas (2008). The present results indicate that the pressure is also consisted in the form of self-similar attached eddies, supporting

Townsend's conjecture directly.

Figure 4.1 illustrates a schematic diagram of the self-sustaining process of attached eddies, including the pressure amplification mechanism obtained in section 3.2. The streamwise meandering streaks (E_1) nonlinearly amplify both rapid (E_{p_r}) and slow pressure fluctuations (E_{p_s}), and they rapidly generate streamwise vortical structures (see cross-correlation functions of C_{vp_r} and C_{vp_s} in figure 3.14 (a)).

4.2 Rapid pressure fluctuations

The rapid pressure fluctuations appear in any kind of linear analysis including the rapid distortion theory. In other words, one may easily think that the evolution of the rapid pressure fluctuations would be mainly determined by a linear theory. However, present results represent that the emergence of rapid pressure fluctuations is indeed strongly correlated to the streamwise meandering streaks, which corresponds to the nonlinear process. Since the energy for streak amplification (the branch from streamwise vortices to streaks) comes from mean shear $\mathrm{d}U/\mathrm{d}y$, the rapid pressure fluctuations (see equation (2.3a)) would be the mediator of the linear lift-up process, (i.e. tilting of streamwise vortices by mean shear):

$$\frac{D\omega_y}{Dt} \sim \frac{dU}{dy}\omega_x, \tag{4.1}$$

where D/Dt is the material time derivative, ω_x and ω_y are the streamwise and wall-normal component of vorticities, respectively (Hwang, 2015; Hwang & Bengana, 2016). This is because the source term of the rapid pressure is essentially the off-diagonal term in the Orr-Sommerfeld-Squire equation (i.e. the term related to the lift-up effect). However, this does not necessarily mean that their amplification should be associated with the linear process, as the nonlinearly

amplified rapid pressure fluctuations decay out during the linear amplification process. Therefore, the main role of the rapid pressure fluctuations in the linear process appears when rapid pressure fluctuations decay out by mediating the lift-up effect. In this respect, a description of rapid pressure fluctuations only with linear theory could be misleading and both linear and nonlinear processes should be taken into account. There are a couple of recent works on pressure fluctuations with linear analysis: e.g. Jiménez (2013) discussed the Orr-mechanism in terms of pressure fluctuations with linear theory, and Luhar *et al.* (2014) used a linear theory for studying dynamics of pressure fluctuations, which essentially yields rapid pressure fluctuations. Current results give some warning to these previous studies based on linearized Navier-Stokes equations.

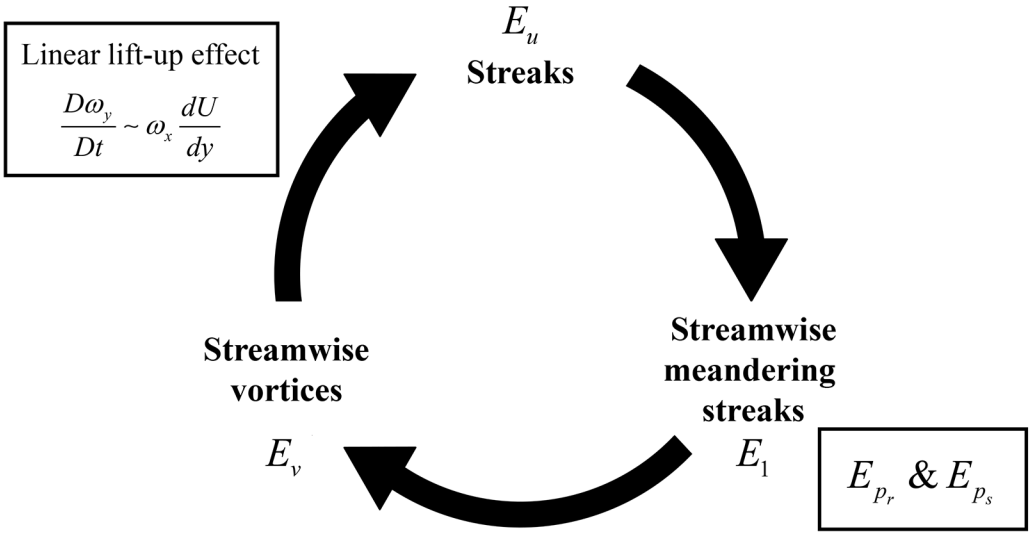

Figure 4.1. A schematic diagram of the self-sustaining process of attached eddies (Hamilton *et al.*, 1995; Hwang & Bengana, 2016), including the amplification process of pressure fluctuations.

Chapter 5

Concluding remarks

In the present study, we have investigated the self-similarity of pressure fluctuations of attached eddies and explored dynamics of both rapid and slow pressure fluctuations. Numerical experiments have been performed to simulate a single self-sustaining attached eddy, extending the scope of previous studies (Hwang, 2015; Hwang & Bengana, 2016). The pressure fluctuations of attached eddies in the logarithmic layer at two different Reynolds numbers ($Re_\tau = 900, 1600$) and various spanwise sizes ($\lambda_{z,0} = 0.375h - h$) have been shown to exhibit self-similarity with respect to the corresponding spanwise size, both statistically and dynamically. These results support the attached eddy hypothesis directly. In particular, dynamics of the pressure fluctuations have been analyzed from the viewpoint of the self-sustaining process of attached eddies in minimal unit simulations (Hamilton *et al.*, 1995; Schoppa & Hussain, 2002; Hwang & Bengana, 2016). Assessing time correlation functions between five energy variables which correspond to the energy of streaks, streamwise meandering streaks, streamwise vortices, rapid pressure fluctuations and slow pressure fluctuations has revealed the pressure amplification process: both rapid and slow pressure fluctuations are amplified together with the meandering motion of the streaks. Current results give some warning to previous studies based on the linear analysis, as it has been revealed that the description of the rapid pressure fluctuations only with linear theory could be misleading.

Through the present study along with previous studies by Hwang (2015) and Hwang & Bengana (2016), statistical and dynamical features of velocity and pressure fluctuations of attached eddies have been unveiled. With these increased understanding of the general organization of coherent structures and their dynamics in wall turbulence, the ultimate goal of the present study is to reveal the mechanism for the maintenance of wall turbulence. This line of research is continued in Part II.

Part II

Scale interactions in turbulent channel flow

Chapter 1

Introduction

Until recently, coherent structures in wall-bounded turbulent flows have been believed to be composed of four characteristic elements (Smits *et al.*, 2011). In the near-wall region, there are near-wall streaks with a spanwise spacing about $100\nu/u_\tau$ (ν is kinematic viscosity and u_τ is wall-shear velocity) and quasi-streamwise vortices, while further from the wall, large-scale motions (LSMs) and very-large-scale motions (VLSMs) emerge (Monty *et al.*, 2009). The LSMs and VLSMs have been identified at sufficiently high Reynolds number flows, and their streamwise size is about $\lambda_x \simeq 2\delta - 3\delta$ and $\lambda_x \simeq O(10\delta)$, where λ_x is streamwise wavelength and δ is boundary layer thickness, respectively (Cossu & Hwang, 2017). However, the general organization of the coherent structures in wall turbulence has begun to be revealed, with recent evidence for attached eddy hypothesis originally suggested by Townsend (1976) (see Introduction in Part I). Based on these evidence, a modern view of coherent structures in wall turbulence is that the smallest attached eddy is composed of near-wall streaks and streamwise vortices, while LSMs and VLSMs correspond to the largest one. Attached eddies in the log layer fill the gap between the inner ($\delta_\nu = \nu/u_\tau$) and outer length scales (δ), in the form of long streaky motions and streamwise vortical structures (Hwang, 2015).

There are different viewpoints on the origin of large-scale coherent structures in the outer layer (Smits *et al.*, 2011). The first one is often referred to

as the bottom-up process, which means that merging of the near-wall structures generate large-scale coherent structures in the outer layer (Kim & Adrian, 1999; Zhou *et al.*, 1999; Toh & Itano, 2005; Guala *et al.*, 2006; Adrian, 2007). However, it has also been reported that the near-wall structures are not an essential ingredient for sustaining outer large-scale structures, which means that large-scale structures have their self-sustaining process (Flores & Jiménez, 2006; Flores *et al.*, 2007; Hwang & Cossu, 2010, 2011; Jiménez, 2013). To address this problem, understanding scale interactions between multi-scale eddies is essential.

Therefore, in the present study, scale interactions in turbulent channel flow are investigated in terms of spectral energy transfer. To clarify scale interactions, we utilize the turbulent kinetic energy (TKE) equation in spanwise wavenumber space. The spanwise wavenumber is considered because a recent study by Hwang (2015) used the spanwise size as a characteristic length scale to isolate the self-sustaining attached eddy, based on the observation of a bimodal streamwise spectral distribution of attached eddies. In this manner, the goal of the present study is to reveal the energy transfer mechanism and ultimately, elucidate the mechanism for maintenance of turbulence.

This paper is organized as follows. In chapter 2, numerical details for a large eddy simulation (LES) of turbulent channel flow is introduced, and verification of the statistics from present LES is followed. In chapter 3, each constituent of TKE equation in wavenumber space is illustrated by premultiplied energy spectra. Then, a detailed analysis of scale interactions and componentwise energy distribution is described. A comprehensive view of the energy transfer mechanism along with self-sustaining and bottom-up processes are provided in chapter 4. This part concludes in chapter 5.

Chapter 2

Numerical method and verification

In the present study, a LES of turbulent channel flow is conducted. $x\,(=x_1)$, $y\,(=x_2)$, and $z\,(=x_3)$ directions indicate the streamwise, wall-normal and spanwise directions, respectively, and $u'\,(=u'_1)$, $v'\,(=u'_2)$, and $w'\,(=u'_3)$ are the corresponding velocity fluctuation components. The Navier-Stokes equations are in the form of the wall-normal component of vorticity ω_y and the Laplacian of the wall-normal velocity $\nabla^2 v$, as in Kim *et al.* (1987). A constant mass flux is imposed by integrating zero wavenumber components of u and w in the form of one-dimensional evolution equations. For the spatial discretization, dealiased Fourier expansions are used in the x and z directions, and Chebychev polynomial expansions are used in the y direction. The time advancement is accomplished by a second-order semi-implicit scheme: a second-order Crank-Nicolson method for the diffusion terms and a third-order Runge-Kutta method for the convection terms. For the subgrid-scale (SGS) model, a dynamic global eddy viscosity model (Lee *et al.*, 2010; Park *et al.*, 2006) is utilized. The computation is carried out in the domain size of $8\pi h(x) \times 2h(y) \times \pi h(z)$ and the number of grid points is $512(x) \times 145(y) \times 128(z)$, where h denotes the channel half-height. The Reynolds number based on the wall-shear velocity u_τ and h is $Re_\tau = u_\tau h/\nu \simeq 1700$ and the grid spacing is $\Delta x^+ = 82, \Delta y^+ = 0.4 - 36.4$ and $\Delta z^+ = 41$ in wall units. Δx^+ and Δz^+ are computed after dealiasing.

The mean streamwise velocity profile and root-mean-square (rms) velocity

and pressure fluctuations are shown in figure 2.2 to verify flow fields from the present LES. All of the statistics of the present LES at $Re_\tau = 1700$ show good agreement with those of direct numerical simulation (DNS) at $Re_\tau = 2000$ by Lee & Moser (2015).

For the purpose of analyzing energy transfer between multi-scale eddies, the evolution equation of TKE is also verified. In a channel flow, the TKE equation is given as (Pope, 2000):

$$\frac{\partial \bar{e}}{\partial t} = -\overline{u'v'}\frac{\mathrm{d}U}{\mathrm{d}y} - \frac{1}{Re}\overline{\left(\frac{\partial u_i'}{\partial x_j}\right)^2} - \frac{\mathrm{d}\overline{ev'}}{\mathrm{d}y} - \frac{\mathrm{d}\overline{p'v'}}{\mathrm{d}y} + \frac{1}{Re}\frac{\mathrm{d}^2\bar{e}}{\mathrm{d}y^2}, \tag{2.1}$$

where $e = \left((u')^2 + (v')^2 + (w')^2\right)/2$ is TKE, t is time, $\overline{\cdot}$ is temporal and spatial averaging in wall-parallel directions, U is the mean streamwise velocity and p' is pressure fluctuations. By considering SGS dissipation for LES, equation (2.1) becomes

$$\frac{\partial \bar{e}}{\partial t} = -\overline{u'v'}\frac{\mathrm{d}U}{\mathrm{d}y} - \frac{1}{Re}\overline{\left(\frac{\partial u_i'}{\partial x_j}\right)^2} - \overline{u_i'\frac{\partial \tau_{ij}'}{\partial x_j}} - \frac{\mathrm{d}\overline{ev'}}{\mathrm{d}y} - \frac{\mathrm{d}\overline{p'v'}}{\mathrm{d}y} + \frac{1}{Re}\frac{\mathrm{d}^2\bar{e}}{\mathrm{d}y^2}, \tag{2.2}$$

where τ_{ij}' indicates SGS stress fluctuation. For fully developed channel flow, equation (2.2) can be rearranged as a following balance equation:

$$0 = P(y) + \varepsilon(y) + \varepsilon_{SGS}(y) + T_{turb}(y) + T_p(y) + T_\nu(y), \tag{2.3}$$

where the terms on the right-hand side indicate turbulence production, viscous dissipation, SGS dissipation, turbulent transport, pressure transport and viscous transport, respectively. Constituents of equation (2.3) are shown in figure 2.3. Each component is shown in the premultiplied form to reflect the amount of energy rate in the logarithmic and outer region properly (Smits *et al.*, 2011).

Since LES is conducted in the present study, summation of the viscous dissipation and SGS dissipation are compared with the viscous dissipation from the DNS. All constituents of the balance equation agree well with those from the DNS.

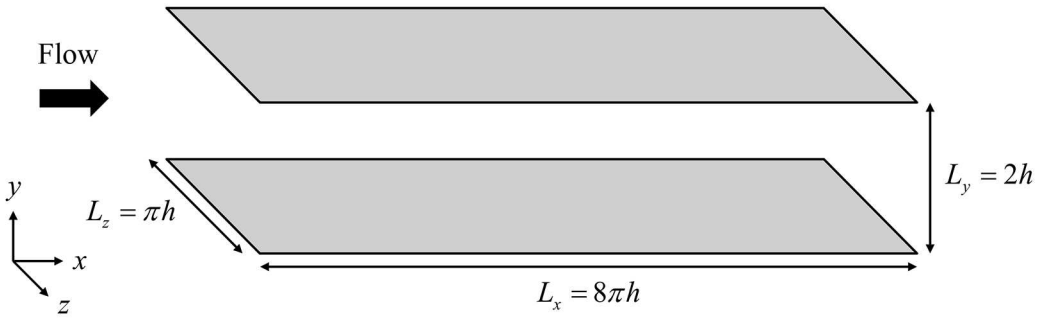

Figure 2.1. Three-dimensional view of the computational domain.

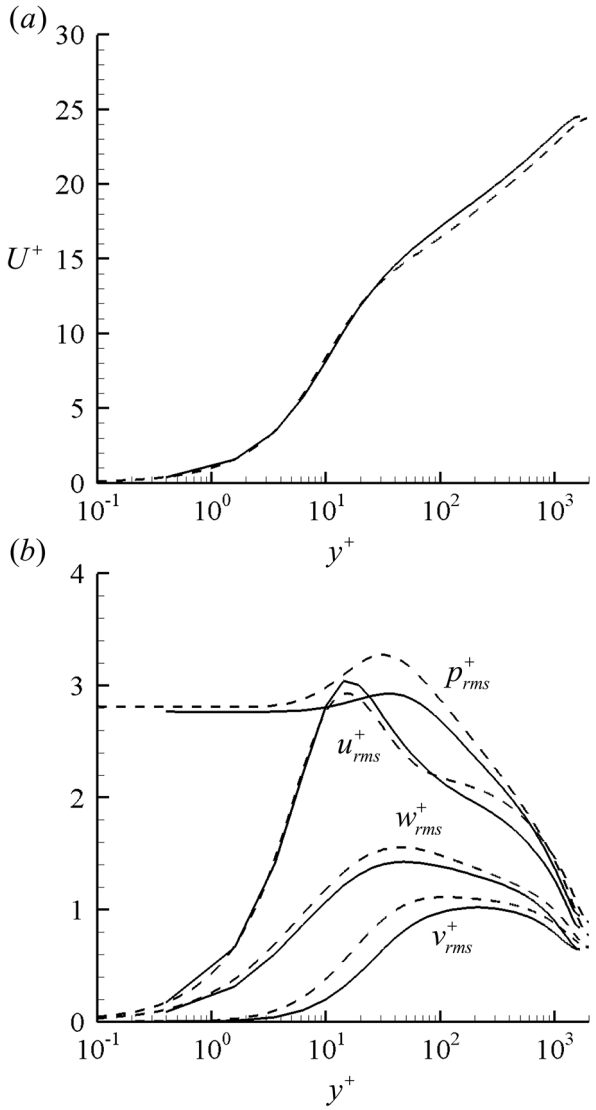

Figure 2.2. (a) Mean streamwise velocity profile and (b) root-mean-square velocity and pressure fluctuations: ——, present LES; - - -, DNS at $Re_\tau = 2000$ (Lee & Moser, 2015).

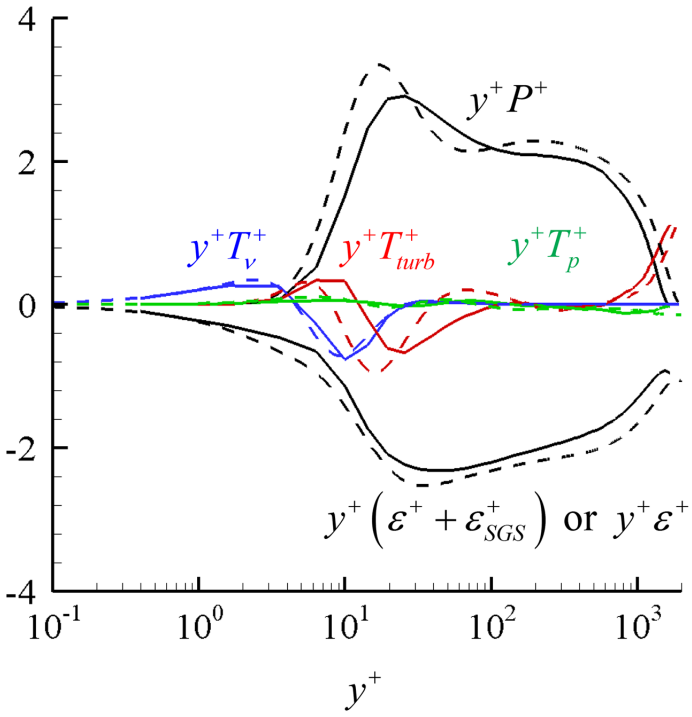

Figure 2.3. Turbulent kinetic energy budget: ——, present LES; - - -, DNS at $Re_\tau = 2000$ (Lee & Moser, 2015).

Chapter 3

Spectral energy transfer and scale interactions

To analyze spectral energy transfer and scale-by-scale interactions, the TKE equation in wavenumber space is explored. The TKE equation is derived from the Navier-Stokes equation, which is Fourier transformed in the z-direction. The resulting balance equation in the wavenumber space is

$$\begin{aligned}
0 &= \widehat{P}\left(y,k_z\right) + \widehat{\varepsilon}\left(y,k_z\right) + \widehat{\varepsilon}_{SGS}\left(y,k_z\right) + \widehat{T}_{turb}\left(y,k_z\right) + \widehat{T}_p\left(y,k_z\right) + \widehat{T}_\nu\left(y,k_z\right) \\
&= \left\langle \mathrm{Real}\left\{ -\overline{\widehat{u}'^{*}_{k_z}\widehat{v}'_{k_z}}\,\frac{\mathrm{d}U}{\mathrm{d}y} \right\} \right\rangle_x + \left\langle -\frac{1}{Re}\overline{\frac{\partial\widehat{u}'_{i,k_z}}{\partial x_j}\frac{\partial\widehat{u}'^{*}_{i,k_z}}{\partial x_j}} \right\rangle_x \\
&+ \left\langle \mathrm{Real}\left\{ -\overline{\widehat{u}'^{*}_{i,k_z}\frac{\partial}{\partial x_j}\left(\widehat{\tau'_{ij}}\right)_{k_z}} \right\} \right\rangle_x + \left\langle \mathrm{Real}\left\{ -\overline{\widehat{u}'^{*}_{i,k_z}\frac{\partial}{\partial x_j}\left(\widehat{u'_i u'_j}\right)_{k_z}} \right\} \right\rangle_x \\
&+ \left\langle \mathrm{Real}\left\{ \frac{\mathrm{d}}{\mathrm{d}y}\left(-\overline{\widehat{p}'_{k_z}\widehat{v}'^{*}_{k_z}}\right) \right\} \right\rangle_x + \left\langle \frac{1}{Re}\frac{\mathrm{d}^2\overline{\widehat{e}_{k_z}}}{\mathrm{d}y^2} \right\rangle_x ,
\end{aligned} \tag{3.1}$$

where $\widehat{\cdot}$ denotes the Fourier coefficients transformed in the z-direction, k_z is the spanwise wavenumber, superscript * is the complex conjugate, $\overline{\cdot}$ is the time average, $\langle\,\cdot\,\rangle_x$ is the spatial average in x-direction, $\partial/\partial x_3 = ik_z$ and $\widehat{e}_{k_z} = \left(\left|\widehat{u}'_{k_z}\right|^2 + \left|\widehat{v}'_{k_z}\right|^2 + \left|\widehat{w}'_{k_z}\right|^2\right)/2$. The summation over the wavenumber k_z of each Fourier component of equation (3.1) corresponds to the each constituent of equation (2.3) in the physical space. It is important to note that the sign of each component of equation (3.1) indicates the TKE gain (positive) or loss (negative),

and the relative magnitude of each component determines the importance of each term.

3.1 One-dimensional spectra

Figure 3.1 shows premultiplied one-dimensional spanwise spectra of the production term. A red dashed line denotes $\lambda_z = 5y$, indicating that the spanwise length scale increases linearly with the distance from the wall (i.e. attached eddies). The linear scaling of the turbulence production spectra and its dominance in making production rate positive are clearly visible.

The premultiplied spectra of dissipation terms are given in figure 3.2. Blue dashed lines are $\lambda_z = 57\eta$, where $\eta = (\nu^3/\varepsilon)^{1/4}$ is the Kolmogorov length scale, indicating the characteristic length scale of dissipative eddies formed from dissipation rate (ε) and kinematic viscosity (ν). Both viscous dissipation and SGS dissipation spectra scale quite well with the Kolmogorov length scale. This implies that eddies involved in the energy cascade would mainly appear between $\eta < \lambda_z < y$.

All transport spectra in figures 3.3 and 3.4 have energy gain (red) and loss (blue), because the transport terms should go to zero when they are integrated over the entire domain. The value of pressure transport spectra in figure 3.3(a) represents that the role of pressure transport is negligible compared to other two transport terms (viscous transport in figure 3.3(b) and turbulent transport in figure 3.4). Also, viscous transport term does its work only in the near-wall region ($y^+ \lesssim 20$), as can be easily deduced considering its nature, and the effect of the viscous part will be decreased as Reynolds number increases. Consequently, the energy production in the log and outer region is mainly balanced by the turbulent transport term in figure 3.4, resulting in large negative trans-

port energy along the line $\lambda_z = 5y$, where the turbulence dissipation and other transport terms would be very weak. Therefore, the energy production in the log and outer layer is mainly sucked by negative turbulent transport energy, and given the mathematical nature of the transport term, that energy is sent to the region where the turbulent transport energy is positive. The area of positive turbulent transport energy can be categorized into two types, either a wide area ($y^+ \gtrsim 25$) or a narrow area ($y^+ \approx 10$). The former may represent the energy cascade, as it appears where the cascade is theoretically expected. Then, that energy would be dissipated as described above (see also dissipation spectra in figure 3.2). However, the latter certainly does not indicate the cascade, as its spanwise length scale is larger than that of attached eddies along the line $\lambda_z = 5y$. The turbulent transport term is analyzed in detail in the following section, to understand the energy transfer mechanism.

3.2 Scale interactions

Considering that the turbulent transport term $\widehat{T}_{turb}(y, k_z)$ in equation (3.1) originates from the nonlinear term of the Navier-Stokes equation, the nonlinear part in $\widehat{T}_{turb}(y, k_z)$ can be rewritten using the convolution theorem:

$$\widehat{T}_{turb}(y, k_z) = \left\langle \text{Real} \left\{ -\overline{\widehat{u}'^{*}_{i,k_z} \frac{\partial}{\partial x_j} \sum_{l+m=k_z} \widehat{u}'_{i,l} \widehat{u}'_{j,m}} \right\} \right\rangle_x , \tag{3.2}$$

which identifies the turbulent transport energy at given wavenumber k_z originating from scale interactions among eddies of wavenumber l and m. With this scale interaction term (equation (3.2)), the origin of turbulent transport energy can be identified, as illustrated in figure 3.5. For a given spanwise length scale $\lambda_{z,0} = 2\pi/k_{z,0}$ and its wall-normal location y_0 in the $y - \lambda_z$ plane, the energy

from wavenumbers l and $m\,(= k_{z,0} - l)$ interactions can be represented in the quadrant. Here, both the horizontal and vertical axes are normalized by $k_{z,0}$, to represent that the region where $l/k_{z,0} > 1$ and $m/k_{z,0} > 1$ (i.e. the first quadrant) shows energy from the interactions among eddies smaller than $\lambda_{z,0}$, while the region where $l/k_{z,0} < 1$ and $m/k_{z,0} < 1$ (i.e. the third quadrant) indicates the energy resulting from the interactions of larger eddies. Remaining quadrants illustrate the energy from the interactions between eddies smaller than $\lambda_{z,0}$ and larger than $\lambda_{z,0}$. In figure 3.6(a), several different $(y_0, k_{z,0})$ points are marked with black dots along the red dashed line ($\lambda_z = 5y$) and blue dashed line ($\lambda_z = 57\eta$), on the turbulent transport spectra. Also, to investigate the weak positive area ($y^+ \approx 10$), the contour level is adjusted as shown in figure 3.6(b). Scale interactions are analyzed for these twelve points marked with black dots.

The origin of negative turbulent transport energy along the red dashed line ($\lambda_z = 5y$) is represented in figure 3.7. Four different $(y_0, k_{z,0})$ points along $\lambda_z = 5y$ in figure 3.6(a) correspond to figure 3.7(a) to (d), in order from left to right. In figures 3.7(a) and (b), the majority of negative turbulent transport energy is generated by the interactions of larger attached eddies (i.e. the third quadrant). As $\lambda_{z,0}$ increases (figures 3.7(c) and (d)), the negative energy still comes from the interactions of the larger attached eddies, but the proportion is reduced because there will be many smaller eddies. Meanwhile, the origin of positive turbulent transport energy, at the locations of four black dots along $\lambda_z = 57\eta$ in figure 3.6(a) is represented in figure 3.8. Positive turbulent transport to the given scale $\lambda_{z,0} = 2\pi/k_{z,0}$ indicates energy influx by interactions between larger eddies (i.e. the third quadrant), which corresponds to the energy cascade. Therefore, the generated energy is sucked by negative turbulent transport originating from nonlinear interactions between larger attached eddies, and is transported to the inertial subrange by the energy cascade where the turbulent transport spectra

are positive. In the same manner, figure 3.9 indicates the origin of weak positive turbulent transport energy marked with black dots in figure 3.6(b). It is clearly shown that most of the energy influx comes from scale interactions between the smaller eddies (i.e. the first quadrant), but there exists the energy influx through eddies smaller than $\lambda_{z,0}$ and larger than $\lambda_{z,0}$ (i.e. the second and fourth quadrant). However, larger eddies (i.e. the third quadrant) only mediate this process.

Figure 3.10 is the same as figure 3.9(a), but the contour level is distributed exponentially. In this way, all of the (l, m) combinations can be illustrated in the quadrant. As the Fourier transform in the spanwise direction is taken for real variables, Fourier coefficients of negative wavenumbers correspond to complex conjugate of those of positive wavenumbers. Therefore, the convolution term in $\widehat{T}_{turb}\,(y_0, k_{z,0})$ (i.e. $\widehat{u}'_{i,l}\widehat{u}'_{j,m}$) can be written as:

$$\begin{cases} \widehat{u}'_{i,l}\widehat{u}'_{j,m}, & 0 \le l, m \le (N_z/2) - 1 \\ \widehat{u}'^{*}_{i,-l}\widehat{u}'_{j,m}, & -(N_z/2) + 1 \le l < 0, 0 \le m \le (N_z/2) - 1 \\ \widehat{u}'_{i,l}\widehat{u}'^{*}_{j,-m}, & 0 \le l \le (N_z/2) - 1, -(N_z/2) + 1 \le m < 0 \\ \widehat{u}'^{*}_{i,-l}\widehat{u}'^{*}_{j,-m}, & -(N_z/2) + 1 \le l, m < 0, \end{cases} \tag{3.3}$$

Therefore, if $k_{z,0}$ is positive, this expression becomes three lines in the quadrant: $l + m = k_{z,0}, -l + m = k_{z,0}$ and $l - m = k_{z,0}$, as shown in figure 3.10. Also, from the relation $\widehat{T}_{turb}\,(y_0, -k_{z,0}) = \widehat{T}^{*}_{turb}\,(y_0, k_{z,0}) = \widehat{T}_{turb}\,(y_0, k_{z,0})$, the case of negative $k_{z,0}$ does not have to be considered separately. However, in order to accurately represent how much energy comes from each quadrant, linear distribution is used for figures 3.7 to 3.9, instead of exponential distributions.

3.3 Componentwise energy distribution

We further investigate equations for each velocity component of TKE to understand the energy redistribution mechanism. Equation (3.1) can be rewritten for each subscript i:

$$
\begin{aligned}
i = 1 : 0 = {} & \widehat{P}\left(y, k_z\right) + \widehat{\Pi}_x\left(y, k_z\right) + \widehat{\varepsilon}_x\left(y, k_z\right) + \widehat{\varepsilon}_{SGS,x}\left(y, k_z\right) \\
& + \widehat{T}_{turb,x}\left(y, k_z\right) + \widehat{T}_{\nu,x}\left(y, k_z\right) \\
= {} & \left\langle \mathrm{Real}\left\{ -\overline{\widehat{u}'^{*}_{k_z} \widehat{v}'_{k_z}} \frac{\mathrm{d}U}{\mathrm{d}y} \right\} \right\rangle_x + \left\langle \mathrm{Real}\left\{ \overline{\widehat{p}'_{k_z} \frac{\partial \widehat{u}'^{*}_{k_z}}{\partial x}} \right\} \right\rangle_x \\
& + \left\langle -\frac{1}{Re} \overline{\frac{\partial \widehat{u}'_{k_z}}{\partial x_j} \frac{\partial \widehat{u}'^{*}_{k_z}}{\partial x_j}} \right\rangle_x + \left\langle \mathrm{Real}\left\{ -\overline{\widehat{u}'^{*}_{k_z} \frac{\partial}{\partial x_j} \left(\widehat{\tau}'_{1j}\right)_{k_z}} \right\} \right\rangle_x \\
& + \left\langle \mathrm{Real}\left\{ -\overline{\widehat{u}'^{*}_{k_z} \frac{\partial}{\partial x_j} \sum_{l+m=k_z} \widehat{u}'_l \widehat{u}'_{j,m}} \right\} \right\rangle_x + \left\langle \frac{1}{Re} \frac{\mathrm{d}^2}{\mathrm{d}y^2} \left(\frac{1}{2} \overline{\left|\widehat{u}'_{k_z}\right|^2} \right) \right\rangle_x ,
\end{aligned} \tag{3.4}
$$

$$
\begin{aligned}
i = 2 : 0 = {} & \widehat{\Pi}_y\left(y, k_z\right) + \widehat{\varepsilon}_y\left(y, k_z\right) + \widehat{\varepsilon}_{SGS,y}\left(y, k_z\right) \\
& + \widehat{T}_{turb,y}\left(y, k_z\right) + \widehat{T}_p\left(y, k_z\right) + \widehat{T}_{\nu,y}\left(y, k_z\right) \\
= {} & \left\langle \mathrm{Real}\left\{ \overline{\widehat{p}'_{k_z} \frac{\partial \widehat{v}'^{*}_{k_z}}{\partial y}} \right\} \right\rangle_x + \left\langle -\frac{1}{Re} \overline{\frac{\partial \widehat{v}'_{k_z}}{\partial x_j} \frac{\partial \widehat{v}'^{*}_{k_z}}{\partial x_j}} \right\rangle_x \\
& + \left\langle \mathrm{Real}\left\{ -\overline{\widehat{v}'^{*}_{k_z} \frac{\partial}{\partial x_j} \left(\widehat{\tau}'_{2j}\right)_{k_z}} \right\} \right\rangle_x + \left\langle \mathrm{Real}\left\{ -\overline{\widehat{v}'^{*}_{k_z} \frac{\partial}{\partial x_j} \sum_{l+m=k_z} \widehat{v}'_l \widehat{u}'_{j,m}} \right\} \right\rangle_x \\
& + \left\langle \mathrm{Real}\left\{ \frac{\mathrm{d}}{\mathrm{d}y} \left(-\overline{\widehat{p}'_{k_z} \widehat{v}'^{*}_{k_z}} \right) \right\} \right\rangle_x + \left\langle \frac{1}{Re} \frac{\mathrm{d}^2}{\mathrm{d}y^2} \left(\frac{1}{2} \overline{\left|\widehat{v}'_{k_z}\right|^2} \right) \right\rangle_x ,
\end{aligned} \tag{3.5}
$$

$$
\begin{aligned}
i = 3 : 0 = \widehat{\Pi}_z\left(y, k_z\right) + \widehat{\varepsilon}_z\left(y, k_z\right) + \widehat{\varepsilon}_{SGS,z}\left(y, k_z\right) \\
+ \widehat{T}_{turb,z}\left(y, k_z\right) + \widehat{T}_{\nu,z}\left(y, k_z\right) \\
= \left\langle \mathrm{Real}\left\{ \overline{\widehat{p}'_{k_z}\left(ik_z\widehat{w}'_{k_z}\right)^*} \right\} \right\rangle_x + \left\langle -\frac{1}{Re}\overline{\frac{\partial \widehat{w}'_{k_z}}{\partial x_j}\frac{\partial \widehat{w}'^*_{k_z}}{\partial x_j}} \right\rangle_x \\
+ \left\langle \mathrm{Real}\left\{ -\overline{\widehat{w}'^*_{k_z}\frac{\partial}{\partial x_j}\left(\widehat{\tau'_{3j}}\right)_{k_z}} \right\} \right\rangle_x + \left\langle \mathrm{Real}\left\{ -\overline{\widehat{w}'^*_{k_z}\frac{\partial}{\partial x_j}\sum_{l+m=k_z}\widehat{w}'_l\widehat{u}'_{j,m}} \right\} \right\rangle_x \\
+ \left\langle \frac{1}{Re}\frac{\mathrm{d}^2}{\mathrm{d}y^2}\left(\frac{1}{2}\overline{\left|\widehat{w}'_{k_z}\right|^2}\right) \right\rangle_x ,
\end{aligned}
\tag{3.6}
$$

where Π_x, Π_y and Π_z indicate pressure strain terms in x, y and z directions. Summation of equations (3.4), (3.5) and (3.6) corresponds to total TKE equation (3.1). This expression yields pressure-strain terms, which is not shown in the total TKE equation. This is because the pressure strain terms sum to zero due to continuity:

$$
\Pi_x + \Pi_y + \Pi_z = p'\frac{\partial u'}{\partial x} + p'\frac{\partial v'}{\partial y} + p'\frac{\partial w'}{\partial z} = 0. \tag{3.7}
$$

Pressure strain terms play an important role in energy redistribution. In turbulent channel flow, the only production occurs in the streamwise direction, from mean shear dU/dy. Through the pressure-strain terms, the streamwise direction loses the energy ($\Pi_x < 0$) then wall-normal and spanwise directions get the energy ($\Pi_y > 0$ and $\Pi_z > 0$) (Pope, 2000). The premultiplied one-dimensional spanwise spectra of the pressure strain terms are shown in figure 3.11. Energy loss in the streamwise direction and gain in the wall-normal and spanwise directions are indicated. It is also interesting to note that all the pressure strain spectra are well aligned with red dashed line ($\lambda_z = 5y$), consistent with the production spectra (see figure 3.1).

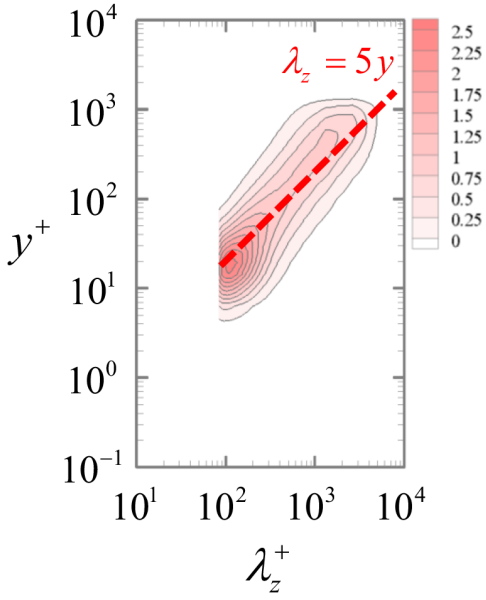

Figure 3.1. Premultiplied one-dimensional spanwise spectra of the production term ($k_z y^+ \widehat{P}^+$).

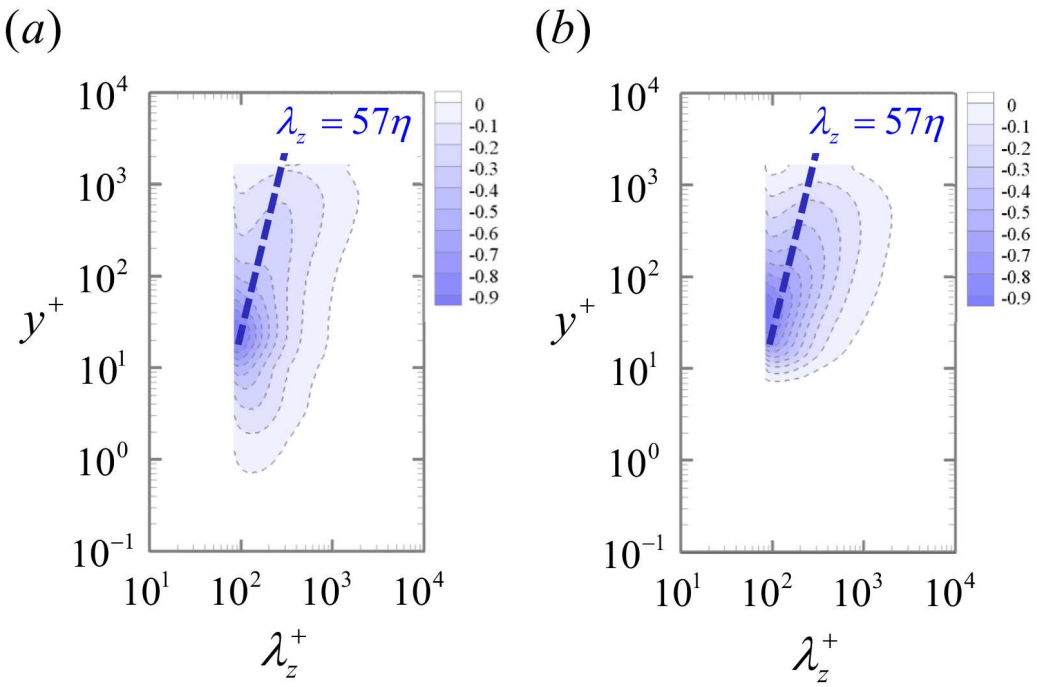

Figure 3.2. Premultiplied one-dimensional spanwise spectra of the (a) viscous dissipation term ($k_z y^+ \widehat{\varepsilon}^+$) and ($b$) SGS dissipation term ($k_z y^+ \widehat{\varepsilon}^+_{SGS}$).

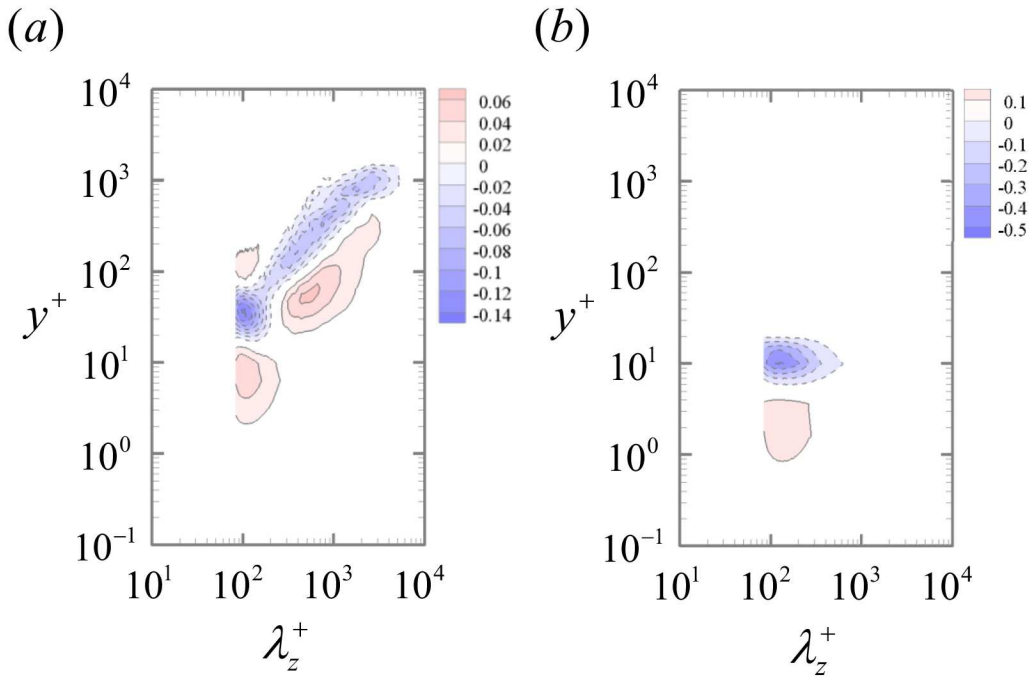

Figure 3.3. Premultiplied one-dimensional spanwise spectra of the (a) pressure transport term ($k_z y^+ \widehat{T}_p^+$) and (b) viscous transport term ($k_z y^+ \widehat{T}_\nu^+$).

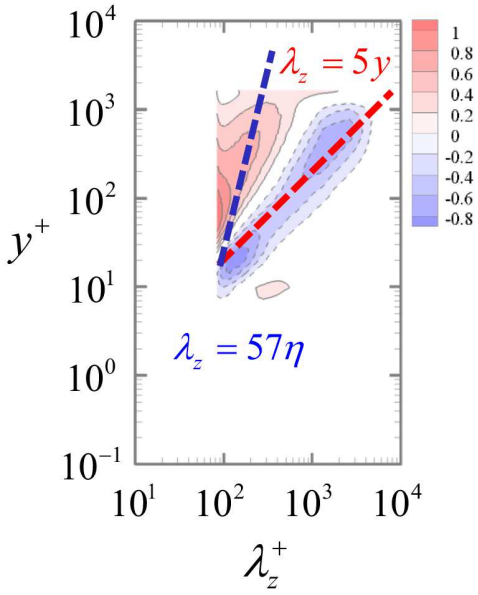

Figure 3.4. Premultiplied one-dimensional spanwise spectra of the turbulent transport term ($k_z y^+ \widehat{T}^+_{turb}$).

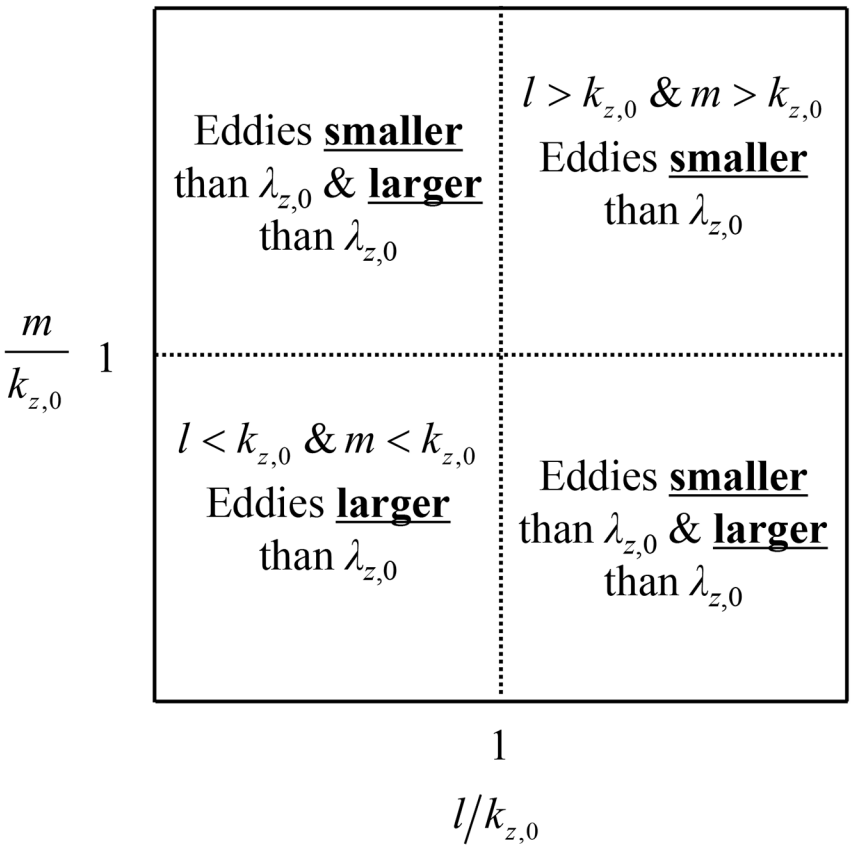

Figure 3.5. Quadrant illustrating the origin of the turbulent transport energy.

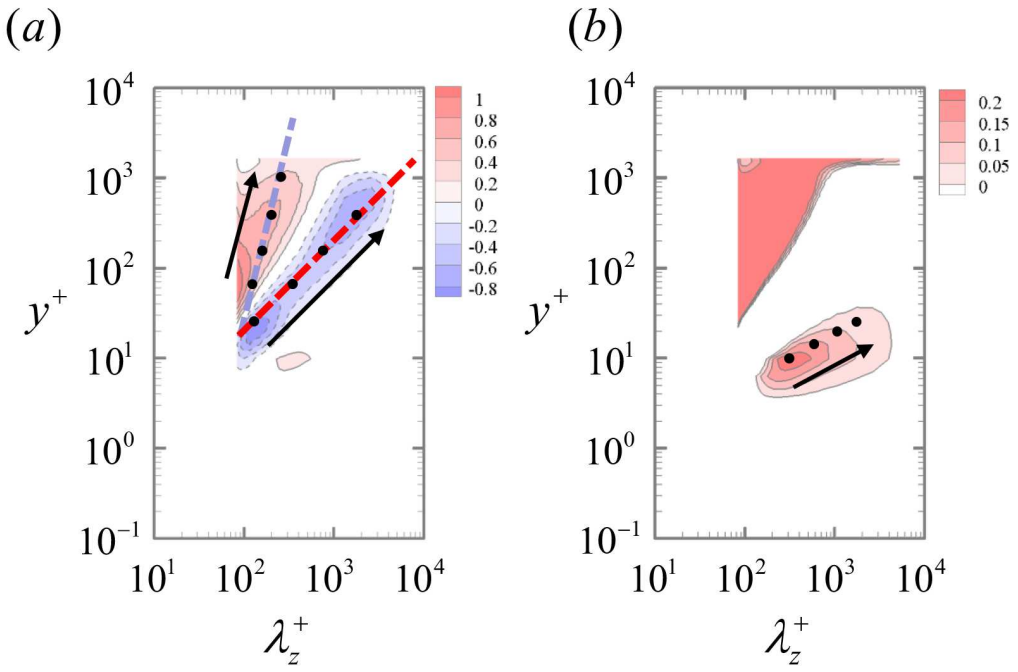

Figure 3.6. Premultiplied one-dimensional spanwise spectra of the turbulent transport term ($k_z y^+ \widehat{T}^+_{turb}$) (i.e. figure 3.4), marked with locations to be analyzed to find the origin of the turbulent transport energy. Both (a) and (b) correspond to figure 3.4, but the contour level is adjusted for (b).

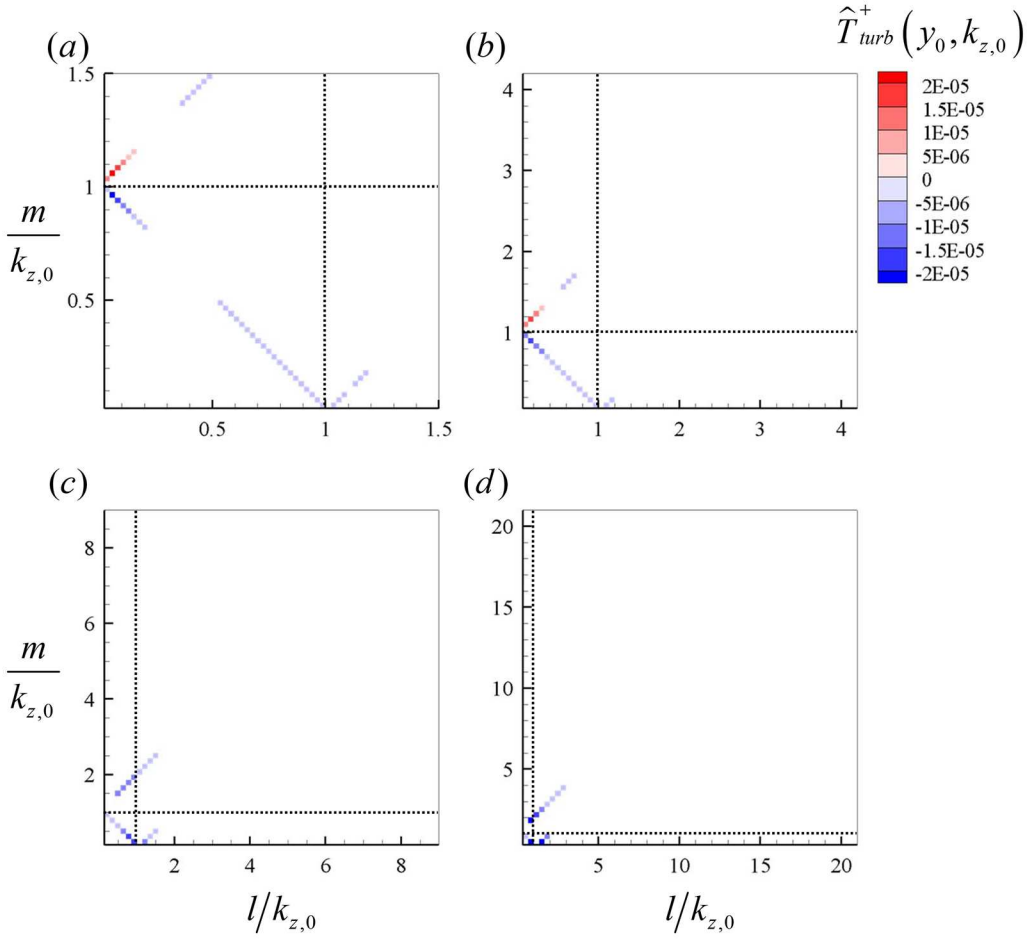

Figure 3.7. The origin of the negative turbulent transport energy along $\lambda_z = 5y$. Each black dot along the red dashed line in figure 3.6(a) corresponds to (a) to (d), in order from left to right.

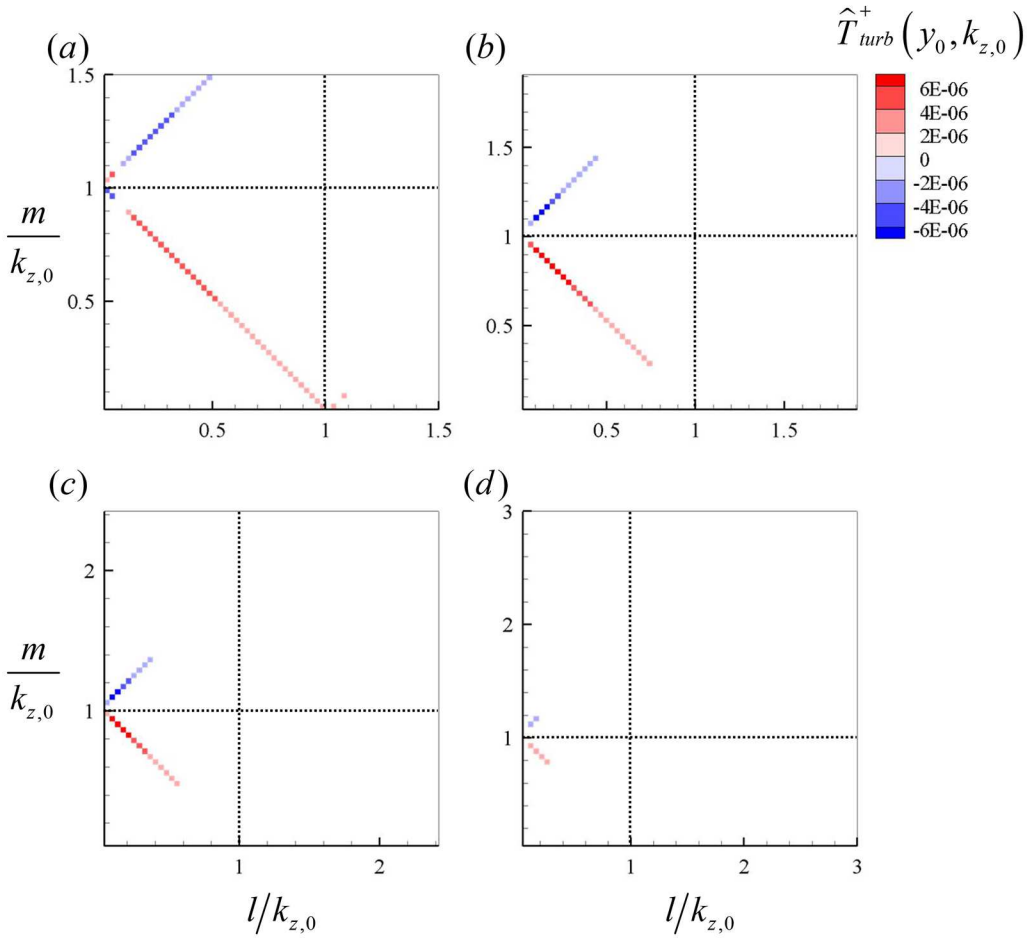

Figure 3.8. The origin of the positive turbulent transport energy along $\lambda_z = 57\eta$. Each black dot along the blue dashed line in figure 3.6(a) corresponds to (a) to (d), in order from left to right.

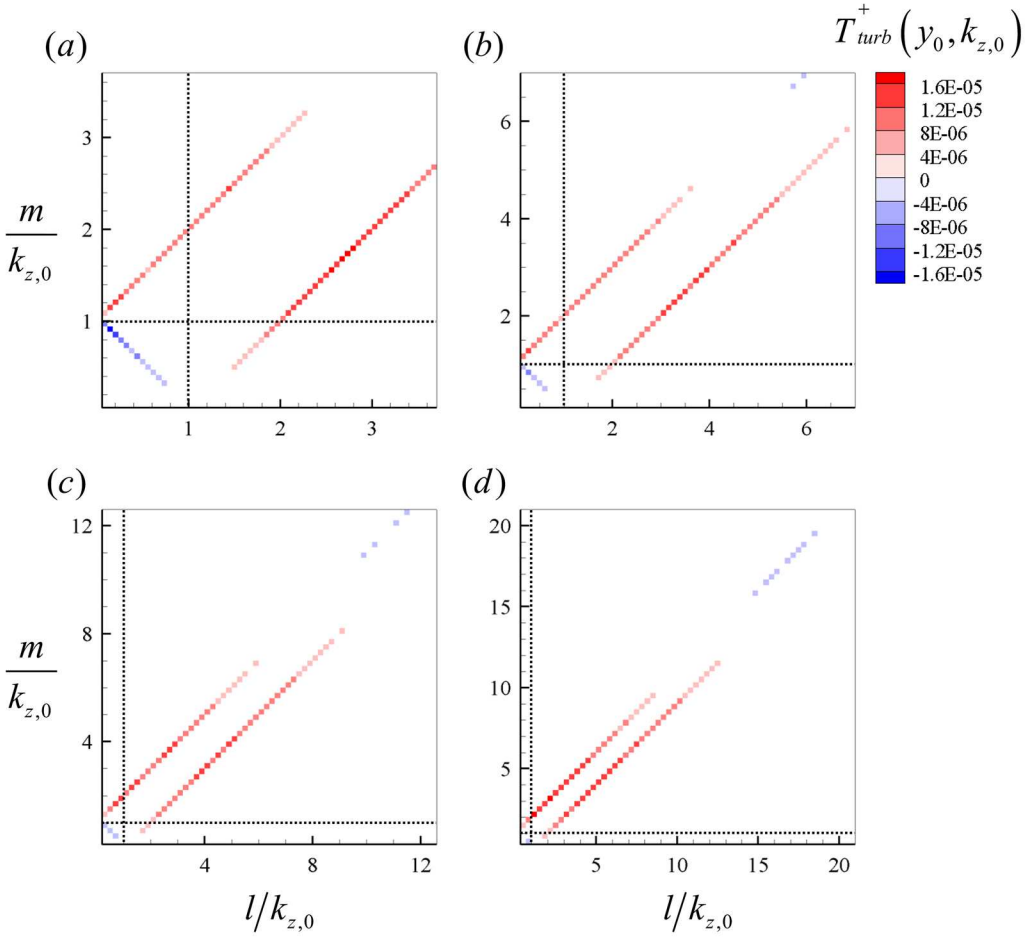

Figure 3.9. The origin of the weak positive turbulent transport energy. Each black dot in figure 3.6(b) corresponds to (a) to (d), in order from left to right.

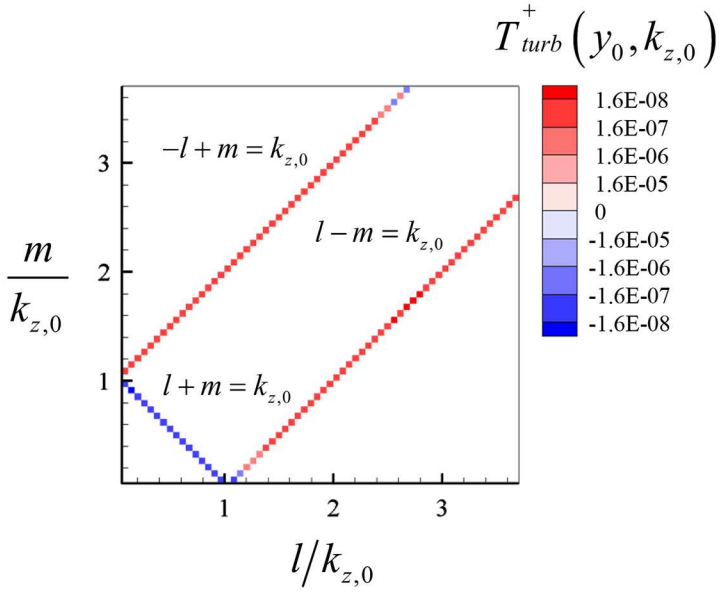

Figure 3.10. Exponential distributions of figure 3.9(a).

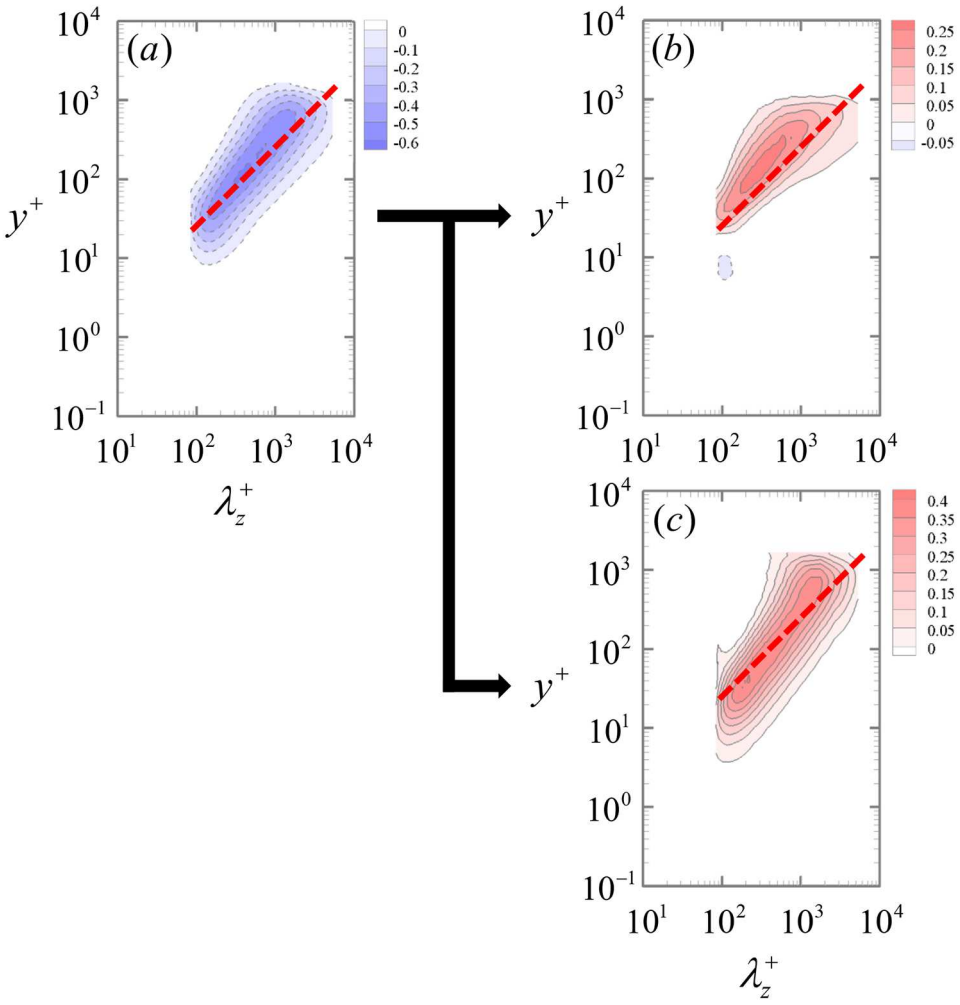

Figure 3.11. Premultiplied one-dimensional spanwise spectra of the pressure strain terms in the (a) streamwise direction ($k_z y^+ \widehat{\Pi}_x^+$), ($b$) wall-normal direction ($k_z y^+ \widehat{\Pi}_y^+$) and ($c$) spanwise direction ($k_z y^+ \widehat{\Pi}_z^+$).

Chapter 4

Discussion

4.1 Componentwise energy transfer and self-sustaining process

Until now, spectral energy transfer has been analyzed by turbulent kinetic energy equation in wavenumber space. Among them, the linear scaling of the production spectra in figure 3.1 implies that the dominant mechanism of turbulence production is the self-sustaining process of attached eddies. Especially, the turbulence production takes place at each length scale which originates from the linear dynamics. This can be inferred by the fact that the contribution of the self-sustaining process goes directly to the production term $\widehat{P}\left(y,k_z\right) = \left\langle \mathrm{Real}\left\{ -\overline{\widehat{u}'^{*}_{k_z}\widehat{v}'_{k_z}}\,\frac{\mathrm{d}U}{\mathrm{d}y}\right\}\right\rangle_x$ at each wavenumber k_z, because the self-sustaining process includes the lift-up effect, (i.e. tilting of streamwise vortices by mean shear):

$$\frac{D\omega_y}{Dt} \sim \frac{dU}{dy}\omega_x, \tag{4.1}$$

where D/Dt is the material time derivative, ω_x and ω_y are streamwise and wall-normal component of vorticities, respectively (Hwang, 2015; Hwang & Bengana, 2016). As the energy production occurs only in the streamwise direction, the linear scaling of the pressure strain spectra in the streamwise direction in figure 3.11 (a) is somewhat predictable. In figures 3.11 (b) and (c), it is clearly shown that the pressure redistributes the energy into other directions and they are also aligned with the linear scaling, showing that the dominant mechanism of energy

redistribution is also the self-sustaining process of attached eddies. From this result, we find an important link with the results in Part I. It has been shown that the temporal dynamics of pressure fluctuations (p') of attached eddies are strongly correlated with streamwise meandering streaks, which can be characterized as $\partial u'/\partial x$. It should be noted that p' and $\partial u'/\partial x$ constitute the pressure strain term in the streamwise direction (see figure 4.1 in Part I). Therefore, the pressure strain spectra show that generated energy via the lift-up effect is redistributed by streak meandering motions ($\partial u'/\partial x$) and pressure fluctuations (p') to cross-streamwise velocities (v and w), which constitute streamwise vortices (ω_x). This energy redistribution mechanism is illustrated in figure 4.1: as streak meanders, streamwise kinetic energy is redistributed to wall-normal and spanwise directions.

4.2 Bottom-up process

The weak positive area in turbulent transport spectra may support the existence of the bottom-up process, as the results from scale-interaction term indicate the energy transfer from small-scale structures to large-scale structures (see figure 3.9). However, it should be noted that this view is only from the energy balance perspective and indeed it does not necessarily mean the merging of small scale structures. Another interesting point is, the wall-normal location of the bottom-up process ($y^+ \approx 10$ in figure 3.4) is consistent with a recent study by Cimarelli *et al.* (2016) with a different method. However, their approach based on the Karman-Howarth equation did not provide how much energy is transported from the near-wall region. However, in the present study, the amount of the bottom-up energy transfer can be quantified, and certainly, it does not seem to be significant compared to the self-sustaining process.

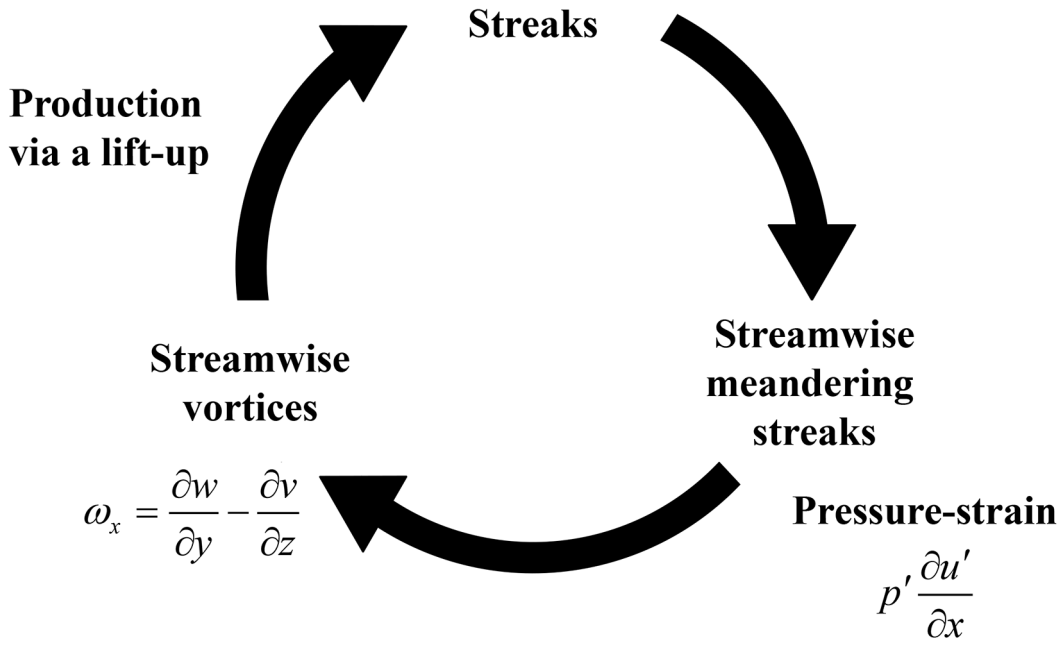

Figure 4.1. Energy redistribution mechanism.

Chapter 5

Concluding Remarks

In the present study, we have clarified the scale interactions and elucidated the energy transfer mechanism, from the perspective of the attached eddy hypothesis. Toward that, a large eddy simulation has been conducted for turbulent channel flow, and each constituent of the turbulent kinetic energy equation in spanwise wavenumber space has been investigated. In particular, scale interactions have been analyzed by turbulent transport term, rearranged by the convolution theorem in wavenumber space. The linear scaling of premultiplied one-dimensional spectra of production term indicates that the lift-up effect in the self-sustaining process of attached eddies at each wavenumber is the dominant mechanism for turbulence production. Meanwhile, in the case of transport terms, the pressure transport energy has a negligible amount of energy and viscous transport term is intense only in the near-wall region. Therefore, the energy production is mainly absorbed by the turbulent transport term and sent to the positive region of the turbulent transport energy. Then the energy is dissipated there, which is shown in the dissipation spectra, scaling well with Kolmogorov length scale. The most important finding in the present study is that the self-sustaining process of attached eddies has been shown to the dominant mechanism for the maintenance of turbulence. Also, the comprehensive view of the energy transfer mechanism has been described. The turbulent kinetic energy at each scale is produced via the lift-up effect and redistributed

by pressure fluctuations and streamwise meandering streaks along a cyclic self-sustaining process of attached eddies. Then, the generated energy is absorbed by negative turbulent transport originating from nonlinear interactions between larger attached eddies and the absorbed energy is transported to the region of positive turbulent transport spectra by the energy cascade. Eventually, the turbulent kinetic energy is dissipated.

References

Adrian, R. J. 2007 Hairpin vortex organization in wall turbulence. *Phys. Fluids* **19**, 041301.

Cimarelli, A., De Angelis, E., Jiménez, J. & Casciola, C. M. 2016 Cascades and wall-normal fluxes in turbulent channel flows. *J. Fluid Mech.* **796**, 417–436.

Cossu, C. & Hwang, Y. 2017 Self-sustaining processes at all scales in wall-bounded turbulent shear flows. *Phil. Trans. R. Soc. A* **375**, 20160088.

del Álamo, J. C. & Jiménez, J. 2003 Spectra of the very large anisotropic scales in turbulent channels. *Phys. Fluids* **15**, L41.

del Álamo, J. C., Jiménez, J., Zandonade, P. & Moser, R. D. 2004 Scaling of the energy spectra of turbulent channels. *J. Fluid Mech.* **500**, 135–144.

Flores, O. & Jiménez, J. 2006 Effect of wall-boundary disturbances on turbulent channel flows. *J. Fluid Mech.* **566**, 357–376.

Flores, O., Jiménez, J. & del Álamo, J. C. 2007 Vorticity organization in the outer layer of turbulent channels with disturbed walls. *J. Fluid Mech.* **591**, 145–154.

Guala, M., Hommema, S. E. & Adrian, R. J. 2006 Large-scale and very-large-scale motions in turbulent pipe flow. *J. Fluid Mech.* **554**, 521–542.

Hamilton, J. M., Kim, J. & Waleffe, F. 1995 Regeneration mechanisms of near-wall turbulence structures. *J. Fluid Mech.* **287**, 317–348.

Härtel, C. & Kleiser, L. 1998 Analysis and modelling of subgrid-scale motions in near-wall turbulence. *J. Fluid Mech.* **356**, 327–352.

Hellström, L. H. O., Marusic, I. & Smits, A. J. 2016 Self-similarity of the large-scale motions in turbulent pipe flow. *J. Fluid Mech.* **792**, R1.

Hutchins, N., Hambleton, W. T. & Marusic, I. 2005 Inclined cross-stream stereo particle image velocimetry measurements in turbulent boundary layers. *J. Fluid Mech.* **541**, 21–54.

Hutchins, N. & Marusic, I. 2007 Evidence of very long meandering features in the logarithmic region of turbulent boundary layers. *J. Fluid Mech.* **579**, 1–28.

Hoyas, S. & Jiménez, J. 2006 Scaling of the velocity fluctuations in turbulent channels up to $Re_\tau = 2003$. *Phys. Fluids* **18**, 011702.

Hwang, Y. & Cossu, C. 2010 Self-sustained process at large scales in turbulent channel flow. *Phys. Rev. Lett.* **105**, 044505.

Hwang, Y. & Cossu, C. 2011 Self-sustained processes in the logarithmic layer of turbulent channel flows. *Phys. Fluids* **23**, 061702.

Hwang, Y. 2013 Near-wall turbulent fluctuations in the absence of wide outer motions. *J. Fluid Mech.* **723**, 264–288.

Hwang, Y. 2015 Statistical structure of self-sustaining attached eddies in turbulent channel flow. *J. Fluid Mech.* **767**, 254–289.

Hwang, Y. & Bengana, Y. 2016 Self-sustaining process of minimal attached eddies in turbulent channel flow. *J. Fluid Mech.* **795**, 708–738.

Hwang, Y. 2016 Mesolayer of attached eddies in turbulent channel flow. *Phys. Rev. Fluids* **1**, 064401.

Jiménez, J. & Hoyas, S. 2008 Turbulent fluctuations above the buffer layer of wall-bounded flows. *J. Fluid Mech.* **611**, 215–236.

Jiménez, J. 2013 How linear is wall-bounded turbulence?. *Phys. Fluids* **25**, 110814.

Kim, J., Moin, P. & Moser, R. 1987 Turbulence statistics in fully developed channel flow at low Reynolds number. *J. Fluid Mech.* **177**, 133–166.

Kim, J. 1989 On the structure of pressure fluctuations in simulated turbulent channel flow. *J. Fluid Mech.* **205**, 421–451.

Kim, K. C. & Adrian, R. J. 1999 Very large-scale motion in the outer layer. *Phys. Fluids* **11** (2), 417–422.

Klewicki, J. C., Priyadarshana, P. J. A. & Metzger, M. M. 2008 Statistical structure of the fluctuating wall pressure and its in-plane gradients at high Reynolds number. *J. Fluid Mech.* **609**, 195–220.

Kline, S. J., Reynolds, W. C., Schraub, F. A. & Runstadler, P. W. 1967 The structure of turbulent boundary layers. *J. Fluid Mech.* **30**, 741–773.

Kunkel, G. J. & Marusic, I. 2006 Study of the near-wall-turbulent region of the high-Reynolds-number boundary layer using an atmospheric flow. *J. Fluid Mech.* **548**, 375–402.

Lee, J., Choi, H. & Park, N. 2010 Dynamic global model for large eddy simulation of transient flow. *Phys. Fluids* **22**, 075106.

Lee, M. & Moser, R. D. 2015 Direct numerical simulation of turbulent channel flow up to $Re_\tau \approx 5200$. *J. Fluid Mech.* **774**, 395–415.

Luhar, M., Sharma, A. S. & McKeon, B. J. 2014 On the structure and origin of pressure fluctuations in wall turbulence: predictions based on the resolvent analysis. *J. Fluid Mech.* **751**, 38–70.

Mansour, N. N., Kim, J. & Moin, P. 1988 Reynolds-stress and dissipation-rate budgets in a turbulent channel flow. *J. Fluid Mech.* **194**, 15–44.

Marusic, I., Monty, J. P., Hultmark, M. & Smits, A. J. 2013 On the logarithmic region in wall turbulence. *J. Fluid Mech.* **716**, R3.

Mason, P. J. & Callen, N. S. 1986 On the magnitude of the subgrid-scale eddy coefficient in large-eddy simulations of turbulent channel flow. *J. Fluid Mech.* **162**, 439–462.

Monty, J. P., Hutchins, N., Ng, H. C. H., Marusic, I. & Chong, M. S. 2009 A comparison of turbulent pipe, channel and boundary layer flows. *J. Fluid Mech.* **632**, 431–442.

Nickels, T. B., Marusic, I., Hafez, S. & Chong, M. S. 2005 Evidence of the k_1^{-1} law in a high-Reynolds-number turbulent boundary layer. *Phys. Rev. Lett.* **95**, 074501.

Park, N., Lee, S., Lee, J. & Choi, H. 2006 A dynamic subgrid-scale eddy viscosity model with a global model coefficient. *Phys. Fluids* **18**, 125109.

Perry, A. E. & Chong, M. S. 1982 On the mechanism of wall turbulence. *J. Fluid Mech.* **119**, 173–217.

Perry, A. E. & Marusic, I. 1995 A wall-wake model for the turbulence structure of boundary layers. Part 1. Extension of the attached eddy hypothesis. *J. Fluid Mech.* **298**, 361–388.

Pope, S. B. 2000 *Turbulent Flows*. Cambridge University Press.

Schoppa, W. & Hussain, F. 2002 Coherent structure generation in near-wall turbulence. *J. Fluid Mech.* **453**, 57–108.

Smits, A. J., McKeon, B. J. & Marusic, I. 2011 High-Reynolds number wall turbulence. *Annu. Rev. Fluid Mech.* **43**, 353–375.

Toh, S. & Itano, T. 2005 Interaction between a large-scale structure and near-wall structures in channel flow. *J. Fluid Mech.* **524**, 249–262.

Tomkins, C. D. & Adrian, R. J. 2003 Spanwise structure and scale growth in turbulent boundary layers. *J. Fluid Mech.* **490**, 37–74.

Townsend, A. A. 1961 Equilibrium layers and wall turbulence. *J. Fluid Mech.* **11**, 97–120.

Townsend, A. A. 1976 *The Structure of Turbulent Shear Flow*. Cambridge University Press.

Tsuji, Y., Fransson, J. H. M., Alfredsson, P. H. & Johansson, A. V. 2007 Pressure statistics and their scaling in high-Reynolds-number turbulent boundary layers. *J. Fluid Mech.* **585**, 1–40.

Zhou, J., Adrian, R. J., Balachandar, S. & Kendall, T. M. 1999 Mechanisms for generating coherent packets of hairpin vortices in channel flow. *J. Fluid Mech.* **387**, 353–396.

난류 채널 유동 내 벽면에 부착된 에디: 압력 섭동과 스케일 상호 작용

서울대학교 대학원
기계항공공학부
조 민 정

요 약

벽 주변의 난류 유동에 존재하는 에디들의 멀티스케일 거동은 난류 유동의 이해를 어렵게 만들어왔다. 하지만 본 연구에서는 Townsend의 벽면에 부착된 에디 가설을 포함하는, 벽 난류의 응집 구조에 대한 현대적인 관점을 가지고 벽 주변의 난류 유동이 가지는 통계적 및 동역학적 특성을 탐구하였다. 이 분석을 통해 얻고자 하는 궁극적인 목표는, 벽 난류가 유지되는 메커니즘을 밝히는 것이다.

1장에서는 주어진 스팬 방향 길이 스케일을 갖는 벽면에 부착된 에디만 남기는 수치 실험을 수행하여 자기-유지되는 벽면에 부착된 에디의 압력 섭동 특성을 조사하였다. 벽면에 부착된 에디의 압력장은 통계적 및 동역학적으로 각각에 대응하는 스팬방향 사이즈에 대해 자기-유사성을 보였으며, 이는 압력 섭동의 구조가 실제로 Townsend의 벽면에 부착된 에디의 형태로 나타나고 있음을 의미한다. 또한, 최소 단위 시뮬레이션으로부터 구한 시간 순서는 빠른(선형) 압력 섭동과 느린(비선형) 압력 섭동 모두 자기-유지 사이클 중 구불구불한 유동 방향 스트릭과 함께 증폭된다는 것을 보여준다.

2장에서는 스케일 간의 상호 작용을 명확히 밝히기 위해 난류 채널 유동의 큰 에디 모사를 수행하였다. 파수 공간에서의 난류 운동 에너지 방정식 구성 요소 각각의 에너지 스펙트럼과 스케일 상호 작용의 분석 결과로부터 에너지 전달 메커니즘에 대한 포괄적인 견해가 서술되었다. 벽면에 부착된 에디의 자기-유지 과정에서 리프트-업 효과에 의해 생성된 난류 운동 에너지는 더 큰 벽면에 부착된 에디들 간의 비선형 상호 작용에 기인한 음의 난류 이동 에너지에 의해 흡수된다. 그리고 흡수된 에너지는 난류 이동 에너지 스

퍽트럼이 양의 값을 갖는 영역으로 에너지 캐스케이드를 통해 이동하여 소산된다. 또한 압력-스트레인 항을 통한 에너지 재분배 메커니즘도 벽면에 부착된 에디의 자기-유지 과정임을 확인하였다. 따라서 벽 난류의 유지를 위한 지배적인 메커니즘은 각 길이 스케일에서, 벽면에 부착된 에디의 자기-유지 과정이다.

주요어: 벽면에 부착된 에디, 압력 섭동, 스케일 상호 작용, 난류 운동 에너지, 자기-유지 과정, 난류 채널 유동
학 번: 2011-22897